Fluid Flow Modeling of Biomimetic Structures

Undergraduate Honors Thesis

Presented in Partial Fulfillment of the Requirements
for Graduation with Honors Research Distinction in the
Department of Mechanical and Aerospace Engineering
at The Ohio State University

By

Samuel G Martin

The Ohio State University

2013

Defense Committee:

Professor Bharat Bhushan, Advisor

Professor Sandip Mazumder

ABSTRACT

The scales of fast-swimming sharks contain riblet structures, micro-grooved surfaces aligned in the direction of fluid flow, that result in water moving efficiently over the surface. In previous studies, these riblet structures have shown a drag reduction effect of up to 10% when compared to a smooth, flat surface; however, these studies left the question of what is occurring around the riblets uninvestigated and they lacked thorough specimen variation. To explore the effects of riblet geometries on drag, three shark-skin inspired riblet configurations were created using ANSYS Fluent, a computational fluid dynamic (CFD) program. These models were created at a Reynolds number of 4200 based on entire channel width using the Large Eddy Simulation (LES) turbulence model. The lateral spacing between riblets was varied and vortex size, vortex location, and drag change was compared. This research found that as riblet lateral spacing was increased, the vortex height and width increased as well. This modeling information will help lead to a better understanding of riblets and allow for improving upon their design. The ultimate goal is to construct riblet designs that optimally reduce drag for various uses such as air, water, and oil flow in pipes and transportation applications of aircraft and ships.

DEDICATION

Dedicated to family and friends, whose unwavering support allowed me to succeed

ACKNOWLEDGEMENTS

I would first like to thank my advisor, Professor Bharat Bhushan, for inviting me to his research laboratory. His guidance and instruction has been infallible, and as a result, I have become a better student and researcher. I would also like to thank Professor Sandip Mazumder for his invaluable computational modeling advice as well as serving on my defense committee.

Additionally, I would like to acknowledge the College of Engineering for their funding support. I would like to recognize the Ohio Supercomputer Center for their support in the form of an allocation of computing time.

TABLE OF CONTENTS

LIST OF FIGURES

LIST OF TABLES

CHAPTER 1: INTRODUCTION

Over the last 3.8 billion years, nature has had time to evolve objects that are efficient, multi-purpose, and use commonly occurring materials. These objects have many uses that can aid humanity and are of commercial interest. Mimicking these biological structures and using them as an inspiration for design is the field of biomimetics. By studying these structures, it may be possible to replicate their functionality [1]. For example, Lotus leaves are leaves with superhydrophobic properties (difficult to wet). The surface of these leaves have high contact angles that allow for water droplets to roll off the surface clearing away dirt particles [2, 3].

The scales of fast-swimming sharks are another object of interest. Sharks are able to move through water quickly with a low energy input even with the drag due to the water. These scales have been found to aid in this movement by reducing drag by nearly 10% [4]. These scales, called dermal denticles (little skin teeth), have riblets (microscopic grooves) aligned parallel to fluid flow as shown in Figure 1.

Riblet technology can be applied to boat hulls, aircraft surfaces, pipe surfaces, and competitive swimwear. In each case, riblets can provide a drag reduction leading to energy savings and performance benefits [5]. Determining optimal riblet geometries has been the goal of much of the previous research due to the numerous potential applications of drag reduction.

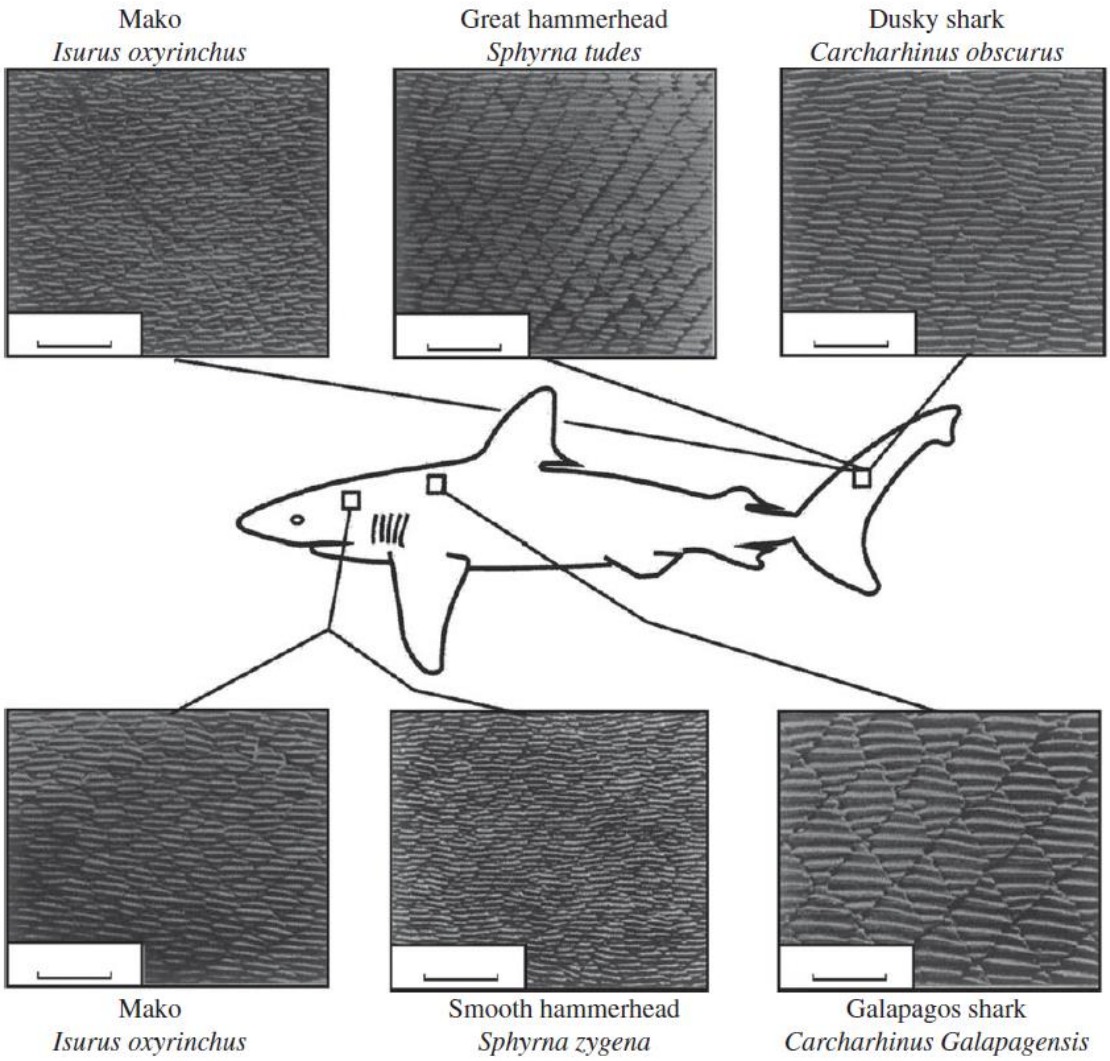

Figure 1: Scale patterns on fast-swimming sharks (Adapted from [6, 7]; scale bar 0.5 mm)

The vortex generation and drag modification effects of riblet structures through computational modeling are the focus of this thesis. First, fluid drag mechanisms are explained with a focus on shark-skin surfaces. Flow characteristics and fluid drag will be explored in this section. Afterwards, the role of riblets on drag and vortices will be discussed. In addition, some previous experimental work on various riblet geometries will be explained.

Next, the computational modeling of riblets will be discussed starting with several verification and validation models. The modeling of shark-skin inspired riblets will then be explored in terms of the integral wall shear stress difference between a smooth surface and a riblet covered surface. In addition, the size, shape, and location of the vortices will be compared across the different configurations. It is the goal that this information will help lead to a better understanding of the role of riblets in drag reduction, and consequently, lead to surfaces with even higher drag-reducing properties.

CHAPTER 2: SHARK SKIN INSPIRED SURFACES

In this chapter, the mechanisms of fluid drag, both pressure and skin friction, are presented. Next, the effects riblets have on drag reduction are introduced followed by various geometries that have been studied.

2.1 Fluid Drag Mechanisms

Fluid drag is commonly split up into two components: pressure drag and skin friction drag. Pressure drag is the drag associated with the energy required to move fluid from in front of the object to behind it. This drag can be reduced with streamlined geometries such as airfoils. Skin friction also called viscous drag is the drag associated with the fluid in closest interaction with a surface. The interaction of the fluid molecules with the surface creates friction and drag. More viscous fluids exhibit higher skin friction drag compared to less viscous fluids due to increased attraction between fluid layers [5, 8].

These two mechanisms can be explained with an example of a person walking through water. Pressure drag would be the drag needed to overcome moving the water in front of one's legs. Skin friction drag would be the drag associated with the fluid interacting with the skin of one's legs.

The laminar and turbulent regime help in explaining fluid drag because turbulence leads to higher viscous drag. In laminar flow, the flow is smooth and uniform whereas in

turbulent flow, the flow is random and chaotic [9]. The transition region from laminar to turbulent flow occurs within a range of Reynolds numbers of 2300-4000 for internal flow and 500,000 for external flow. The dimensionless Reynolds number (Re) is a ratio of inertial forces to viscous forces and can be calculated from Eq. (1) where ρ is the fluid density, μ is the dynamic viscosity, V is the fluid mean flow velocity, and D is the characteristic length. For internal flow, D is the hydraulic diameter.

$$\mathrm{Re} = \frac{\rho \mathrm{V} \mathrm{D}}{\mu} \tag{1}$$

In turbulent flow, the molecules rotate and translate in the viscous sublayer, the layer closest to the surface. These vortices rotate in the streamwise direction (along the axis of mean velocity direction) and interact with the surface as well as nearby vortices. As they interact, vortices tangle and are ejected from the viscous sublayer into the outer boundary layers. The interaction of these vortices can create transient velocity vectors in the cross-stream direction with magnitudes as large as the streamwise direction. These various interactions increase momentum transfer which leads to higher drag [8, 9]. Reducing this momentum transfer is a method of reducing drag.

2.2 Role of Riblets in Drag Reduction

The scales of fast-swimming shark skin are called dermal denticles. These scales have riblets (microscopic grooves aligned parallel to fluid flow) which aid in decreasing momentum transfer and therefore overall drag. The riblets have a size and shape that varies between shark species; however, they all function in a similar manner in reducing

drag. Even though the effects of riblet drag reduction are reproducible, the mechanisms behind this phenomenon are not fully understood.

It is thought that riblets reduce drag in several ways. One, riblets are barriers to vortices settling within the valleys and instead lift the vortices from the surface. Instead of vortices and higher velocity fluid interacting with the entire surface, they only interact with the riblet tips. These tips experience high shear stress, whereas the majority of the riblet surface experiences lower shear stresses due to the lower velocity fluid. Over the entire riblet surface, there is an overall lower shear stress than an equivalent flat surface. Secondly, riblets pin the vortices which decreases cross-stream translation and ejection. In the riblet valleys, there is less dynamic activity with the majority of the velocity in the streamwise direction. This dampening effect leads to a reduction in momentum transfer and therefore drag [4, 5, 7, 10-12].

In Figure 2, a flow visualization of vortices interacting with a flat plate and a riblet surface is shown. These images are of smoke burned from atomized oil in air under two different velocities for a drag decreasing and increasing case. The dimensionless riblet spacing s^+ and height h^+ parameters are shown with their derivation described in the following section. This figure suggests that choosing appropriate parameters for riblet spacing will lead to a drag reduction benefit by lifting and pinning the vortices [12].

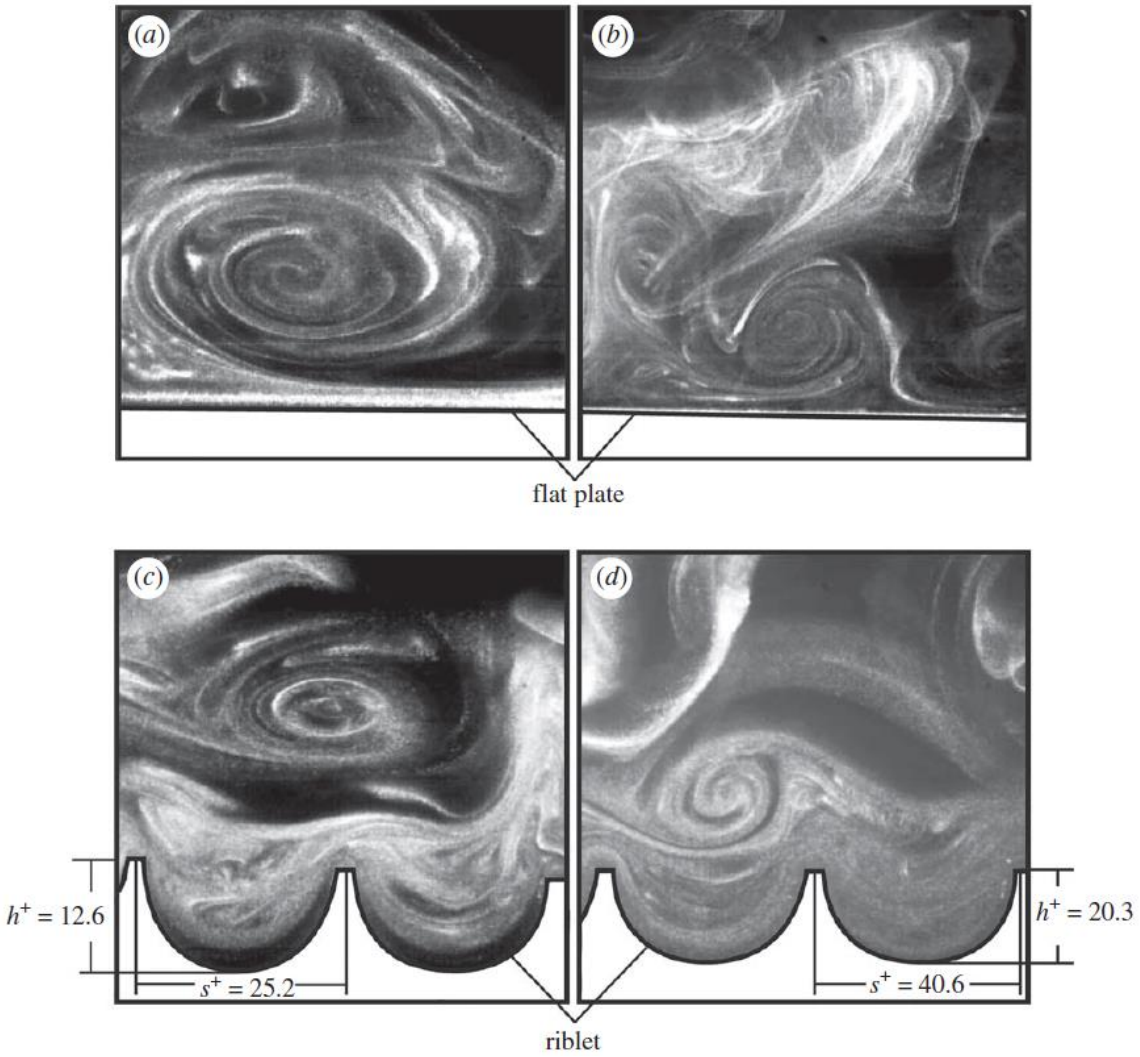

Figure 2: Turbulent flow visualization of vortices interacting with flat and riblet surfaces in a vertical cross-section: (a) drag decreasing case V=3ms^{-1}; (b) drag increasing case V=5ms^{-1}; (c) drag decreasing case V=3ms^{-1}; (d) drag increasing case V=5ms^{-1}; Adapted from [12]

2.3 Riblet Geometries

There are various riblet geometries on different shark species and even different riblet geometries on the same shark species that vary depending based on the location of the scale. Because of the numerous shark riblet geometries, various shark-skin inspired riblet geometries have been explored. An optimal riblet geometry needs to lift and pin the

vortices while balancing the increase in surface area to optimally reduce drag. In the turbulent regime, because fluid drag generally increases dramatically with an increase in wetted surface area, using a profile with too much surface area will increase drag [5].

To describe these riblet geometries, various nondimensional parameters based on wall units are used for lateral spacing s^+, height h^+, and thickness t^+. These parameters are defined in Eq. (2) where v is the kinematic viscosity and V_τ is the wall shear stress velocity [4, 7, 9]. From kinetic energy, the wall shear stress velocity can be calculated using Eq. (3) where τ_0 is the wall shear stress.

$$s^+ = \frac{sV_\tau}{\nu}, \quad h^+ = \frac{hV_\tau}{\nu}, \quad t^+ = \frac{tV_\tau}{\nu} \tag{2}$$

$$V_\tau = \left(\frac{\tau_0}{\rho}\right)^{1/2} \tag{3}$$

The coefficient of skin friction (C_f) can be described by the Fanning friction factor formula, Eq. (4) where V is the bulk fluid velocity [8, 13].

$$C_f = \frac{2\tau_0}{\rho V^2} \tag{4}$$

Combining Eq. (2-4) and solving for the nondimensional riblet parameter results in Eq. (5) [13, 14]. This research uses the reported C_f value and Eq. (5) to nondimensionalize the parameters.

$$s^+ = \sqrt{\frac{C_f}{2}}\frac{sV}{\nu}, \quad h^+ = \sqrt{\frac{C_f}{2}}\frac{hV}{\nu}, \quad t^+ = \sqrt{\frac{C_f}{2}}\frac{tV}{\nu} \tag{5}$$

Both two- and three-dimensional shark-skin inspired riblets have been previously tested. Two-dimensional riblets have a continuous profile along the streamwise direction

whereas three-dimensional riblets are segmented along the profile. The most commonly tested riblet geometries are symmetrical two-dimensional sawtooth, scalloped, and blade profiles [7, 15-19]. The results for these geometries are presented in Figure 3. The percentage drag change is calculated using $\Delta\tau/\tau_0$ where $\Delta\tau$ is the change in integral wall shear stress between the riblet surface and the smooth surface (τ_0). It can be observed that even after choosing appropriate riblet dimensions for each geometry, the blade profile provided the greatest drag reduction at 9.9% compared to 5% and 6.5% for sawtooth and scalloped riblet geometries. For the three geometries, an s^+ value near 15 resulted in the greatest drag reduction. As shown in Figure 2, the vortices have a diameter of approximately 35-50 wall units [7, 19]. With the s^+ spacing near 15, several riblets can be in contact with a vortex to lift and pin it. When the s^+ spacing becomes too large (Figure 2d), a vortex will not be in contact with a couple riblet tips; therefore, a vortex would not be lifted or pinned as much and would lead to a drag increasing case.

Three-dimensional riblets include aligned, segmented blade [20]; offset, segmented blade [7]; offset, three-dimensional blade [7]; and three-dimensional shark-skin replicas [18, 21, 22]. Three-dimensional riblets were studied to better approximate shark skin and to explore other methods of drag reduction; however, no improvement in drag reduction over two-dimensional geometries was seen. Figure 4 shows the results for segmented and continuous blade geometries with the continuous profile exhibiting greater drag reduction. It has been concluded that it is highly unlikely that three-dimensional riblets using segmented riblets will significantly lead to performance increases over continuous two-dimensional riblet designs [5].

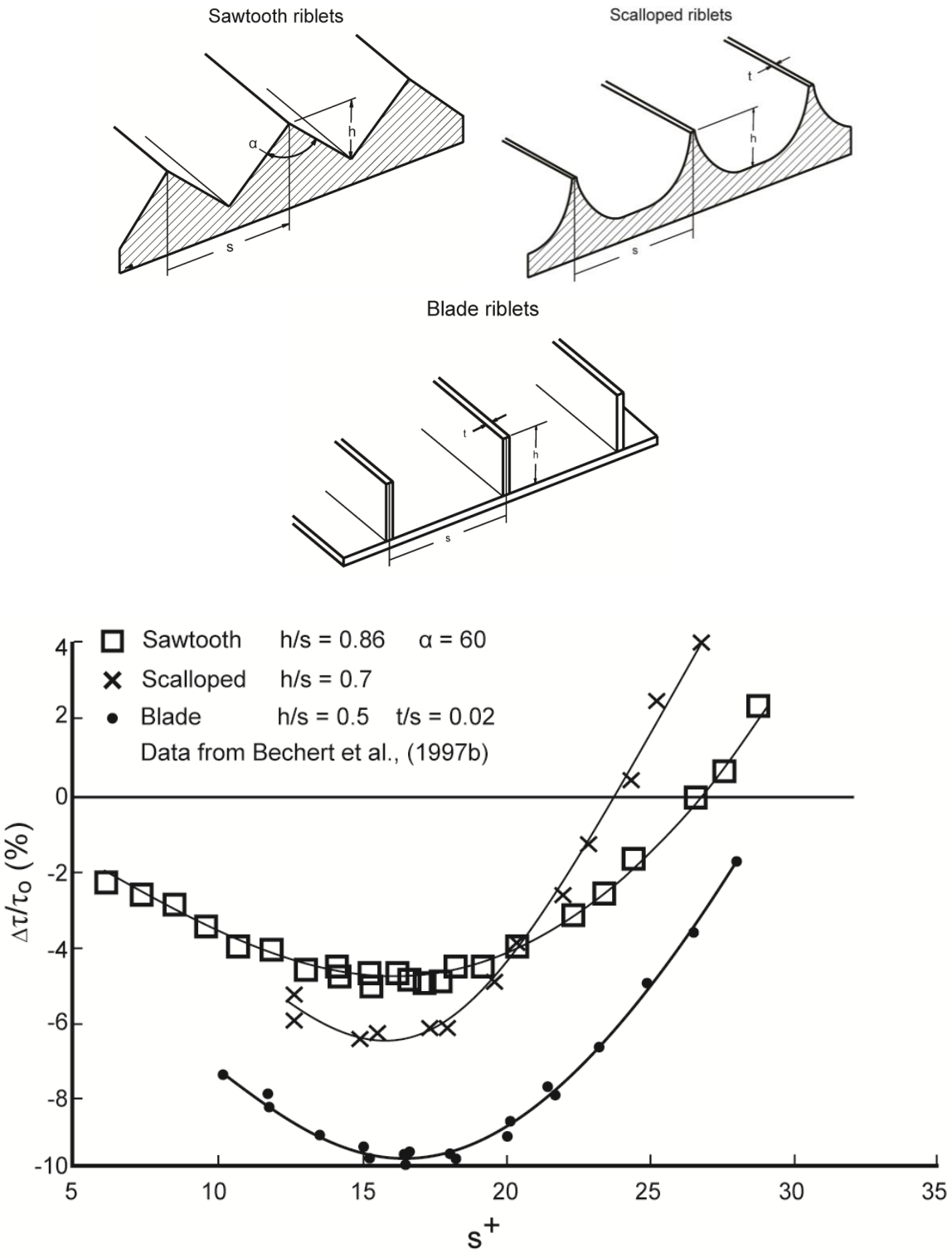

Figure 3: Schematic representation of riblet geometries; Turbulent wall shear stress compared to smooth plate reference for various riblet geometries and s^+ spacing; Adapted from [4]

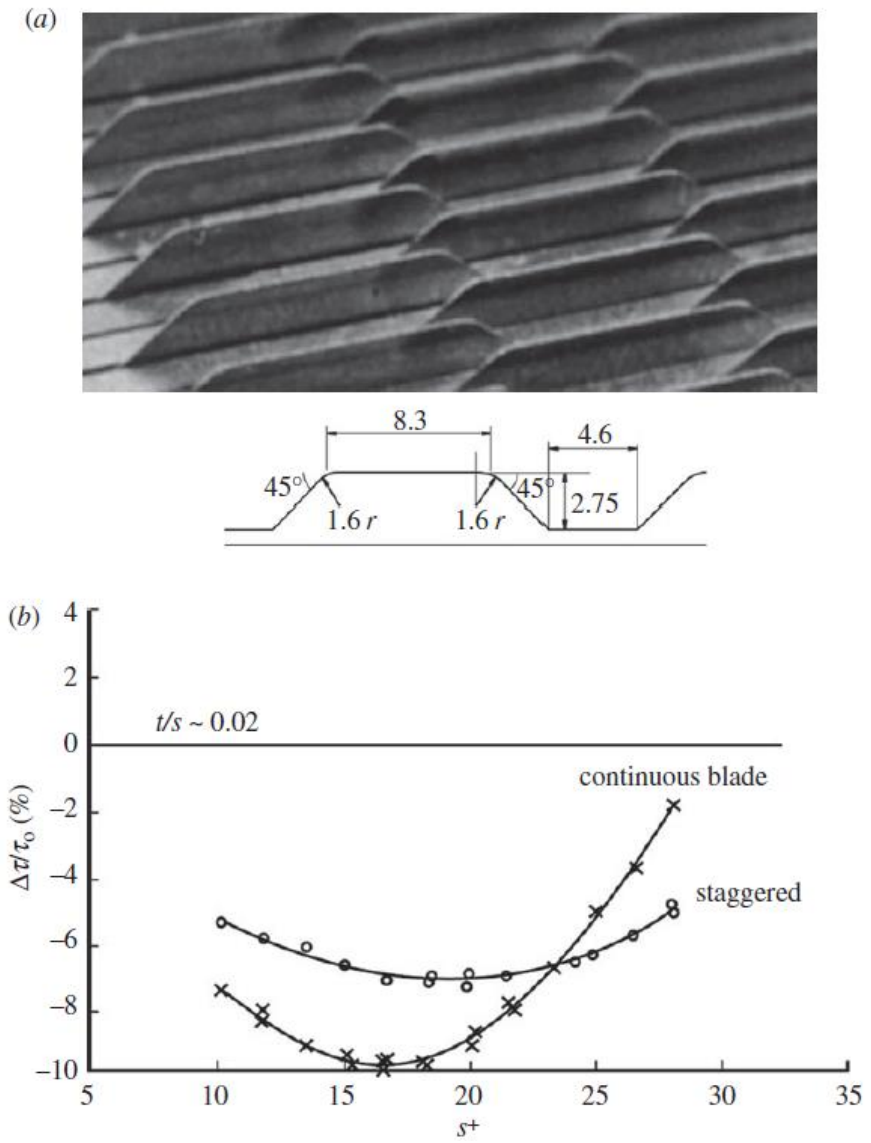

Figure 4: Comparison of drag reduction over optimum continuous blade riblets with optimum segmented trapezoidal blade riblets: (a) Segmented riblets staggered as shown; (b) Drag reduction for continuous blade $(h/s = 0.4)$ and staggered blade $(h/s = 0.5)$; Adapted from [4, 7]

2.4 Riblet Applications

There are several possible commercial applications for riblet technology: competitive swimsuits; air, water, and oil pipe flow; and transportation applications such as aircraft and ships. Currently, riblet technology has been employed in competitive

swimwear such as the Speedo Fastskin swimsuit to decrease drag by several percent over other swimsuits. Applying riblets to the inside of pipes would decrease the drag and allow for the fluid to travel through faster [5]. Riblets could also be applied to the hull of ships and aircraft for fuel savings. According to [23], 70% of an aircraft can be covered by riblets with the other 30% needed to be left normal for visibility and high-wear locations. The 70% covered by riblet technology would provide a 3% drag reduction and therefore a 3% savings in fuel costs. According to Airlines for America [24], in 2012 U.S. passenger and cargo airlines used $15.7 billion gallons of jet fuel at a cost of $46.4 billion. With a 3% drag reduction, there would be $1.4 billion in fuel savings. Based on these examples, riblet technology has many uses and benefits in the commercial sector.

CHAPTER 3: OBJECTIVE AND APPROACH

In this chapter, the computational fluid dynamic (CFD) software is introduced. Afterwards, the test cases for verification and validation purposes will be described. Following these test cases, the shark-skin inspired riblet configurations will be presented. The methodology used to setup the models will be explained including the geometry, mesh generation, and model setup.

It is the goal that the verification and validation models will show that the software is working correctly and that the CFD models were correctly set up. The riblet models will allow for the drag difference to be compared as well as show vortex shape, size, and location.

3.1 Computational Fluid Dynamic Software

The software that was chosen for this research was ANSYS Fluent 14.0 [25]. This software is a popular commercial CFD package that has undergone many revisions over the years and been rigorously tested. Furthermore, this package contains all the resources needed to do a fluid analysis such as geometry, mesh, model, and post-processing components; therefore, using Fluent negates the need to learn and use multiple software programs allowing one to more quickly begin CFD work.

In addition, Fluent is extremely modular and versatile allowing the user to choose between various mesh configurations and model setup. It is capable of using structured

and unstructured mesh types. For model setup, there are various models that range in complexity from laminar to Large Eddy Simulation. There are many other parameters that allow for a great deal of control over the simulation.

3.2 Verification and Validation Models

There were four different cases that were used to demonstrate that the software was working correctly and that I can correctly set up the models. These cases were a two-dimensional cylinder, a driven cavity, a backward facing step, and a three-dimensional square cylinder. For each model, the results were compared to published results.

For the driven cavity and backward facing step test cases, the published literature nondimensionalizes the data set using Eq. **(6)-(8)**. The nondimensional terms are shown with an '*' symbol. The nondimensional u- and v-velocity are found using Eq. **(6)**. There are two ways to nondimensionalize pressure. When dynamic effects are dominant, Eq. **(7)** left is used; when viscous effects are dominant, Eq. **(7)** right is used. Vorticity (ω) using Eq. **(8)** is nondimensionalized using a reference length (L_{ref}) and a reference velocity (U_{ref}).

$$u^* = \frac{u}{U_{ref}}, \quad v^* = \frac{v}{U_{ref}} \tag{6}$$

$$P^* = \frac{L_{ref}P}{U_{ref}\mu}, \quad P^* = \frac{P}{\rho U_{ref}^2} \tag{7}$$

$$\omega^* = \frac{L_{ref}\omega}{U_{ref}} \tag{8}$$

3.2.1 Two-Dimensional Cylinder

The first case was a two-dimensional cylinder in crossflow at a Reynolds number of 1, 20, and 100. The setup can be seen in Figure 5. The outer boundary was set 100 times larger than the cylinder diameter. There were 200 divisions around the outer boundary and 200 divisions going from the outer boundary to the cylinder walls with a 500 bias toward the cylinder walls. The solver was a steady pressure-based viscous laminar model. The solution methods used were the SIMPLE scheme, least squares cell based gradient, standard pressure, and second order upwind momentum. The model was run to residuals of 10^{-6}. To verify the results, the reported drag coefficient was compared to published results of drag coefficient versus Reynolds number.

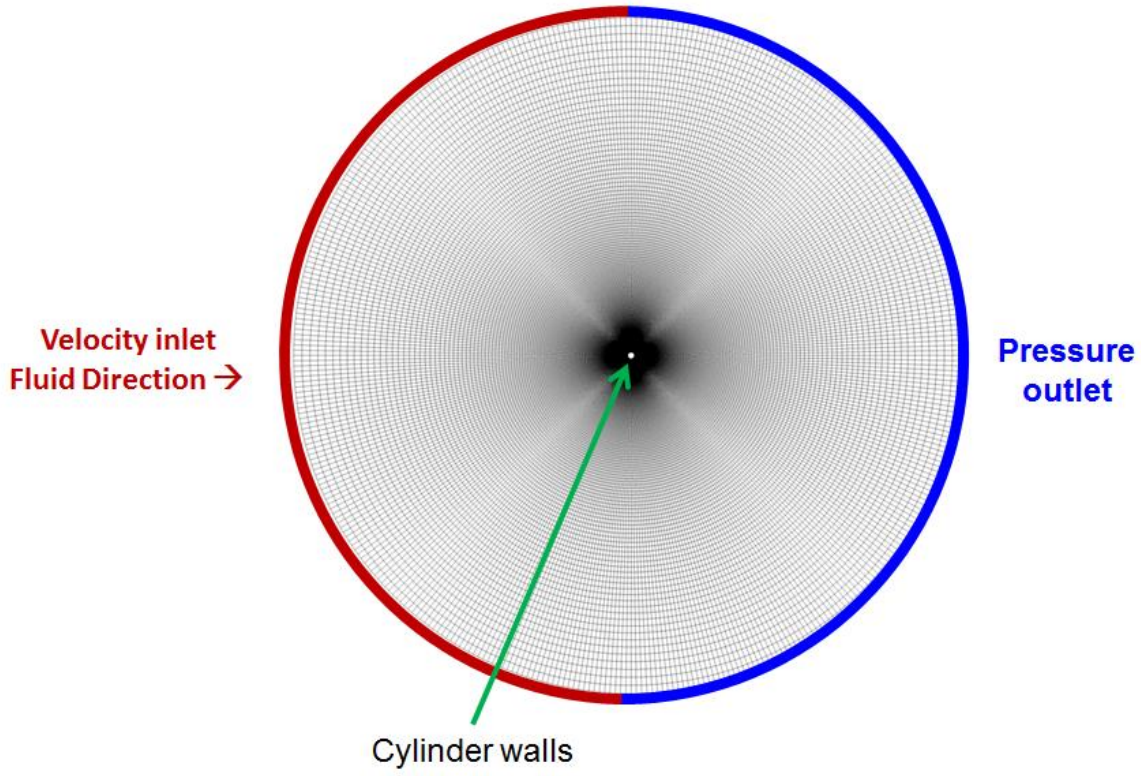

Figure 5: Two-dimensional cylinder setup

3.2.2 Driven Cavity Flow

The driven cavity flow problem is a well-documented test case for various Reynolds numbers. In this case, a square model with four walls is created. The top wall is called the moving lid with a velocity in the positive x-direction (see Figure 6) with the other three walls stationary.

For this model, the Reynolds number is defined by Eq. **(9)** where L is the length of one of the walls. This model was run at a Reynolds number of 1000 until all the residuals decreased to 10^{-6}. A grid size of 320x320 elements was used because this mesh size matched well with the literature and would become too computationally time consuming if increased further. Data will be presented for u-velocity, v-velocity, pressure, and vorticity contours plots and are compared to [26], who used a grid of 1024x1024 elements, and [27], who used a grid of 129x129 elements.

$$\text{Reynolds Number} = \text{Re} = \frac{\rho u_{\text{lid}} L}{\mu} \tag{9}$$

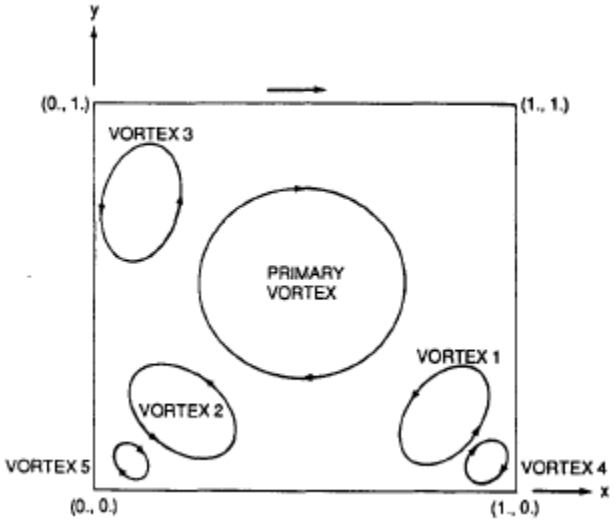

Figure 6: Driven cavity model with vortex locations [28]

3.2.3 Backward Facing Step

The backward facing step problem is another well-documented test case for various Reynolds numbers. In this case, flow comes in a region and travels over a sudden increase in area (see Figure 7). This step creates a recirculation region with the reattachment length compared in the literature. The top and bottom surfaces are modeled as walls with the right surface modeled as a pressure outlet.

For this model, the Reynolds number is defined by Eq. (10) where *D* has different definitions within the literature for a Reynolds number based on step, channel, or inlet height. To match the data from [29, 30], *D* was taken to be the total height (*H*) of the inlet region and step region. This model was run in the laminar regime at a Reynolds number of 800 and the turbulent regime at Reynolds numbers of 93,000 and 210,000. These Reynolds numbers were chosen to be compared to [31, 32].

$$\mathrm{Re} = \frac{\rho u_{in} D}{\mu} \tag{10}$$

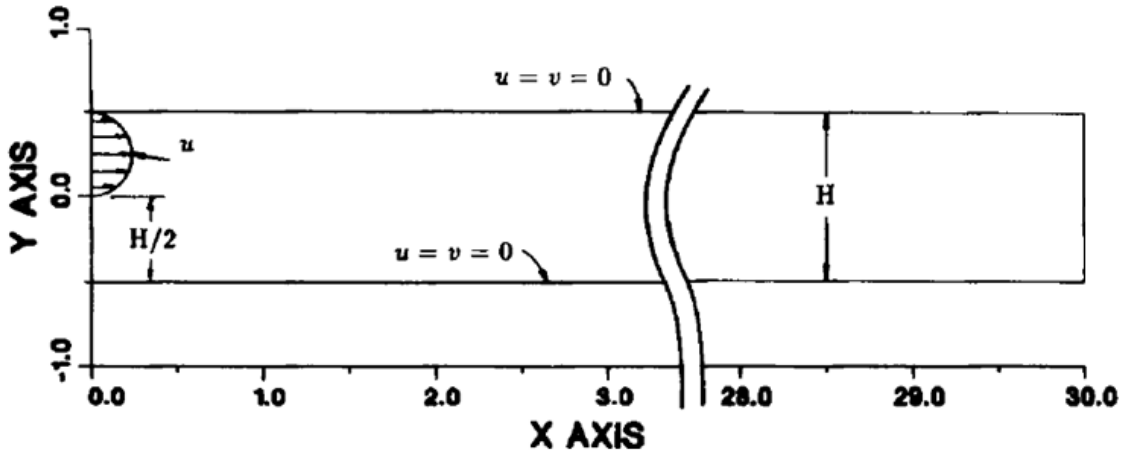

Figure 7: Backward facing step geometry [30]

For the Reynolds number case of 800, a laminar model was used. The model was run until the residuals decreased to 10^{-6}. The geometry was the same as Figure 7 except with an extended inlet region. Due to the requirement of having a parabolic velocity profile, the inlet flow region was extended far enough so that a fully-developed laminar profile would cross the step transition. The length of this region (l_e) was calculated using Eq. (11) where d is the diameter of the inlet region [8]. The fluid velocity was verified to have a parabolic profile in the region shortly before the step. The maximum velocity was within 0.126% for $1.5U_{in}$ velocity, corresponding to the maximum velocity for a laminar parabolic profile.

$$l_e = 0.06 d \mathrm{Re} \tag{11}$$

The computational domain had 80 elements in the y-direction and 1600 elements from the step to the pressure outlet with a bias toward the step of 10. The inlet region had 800 elements with a bias toward the step of 20. These numbers were chosen to be similar to the mesh from [30]. Several reattachment points and the *u*- and *v*-velocity at x = 7 and 15 were compared to [29, 30].

For the of 93,000 and 210,000 Reynolds number cases, these models were run with the RNG k-epsilon turbulence model. These models were run to residuals of 10^{-6}. Because these models did not require a parabolic velocity profile at the step, the model geometry was changed to decrease the mesh size and therefore the solution time. Instead of the inlet region of length l_e, the inlet region was shortened to have an length of $x/H = 2$. At the inlet, 5% turbulence intensity was prescribed for the hydraulic diameter. The reattachment length was compared to [31, 32].

3.2.4 Three-Dimensional Square Cylinder

Another test case was run using the Large Eddy Simulation (LES) model for the flow over a three-dimensional square cylinder. This simulation is a well-documented experimental and computational case [33-35].

The flow that is modeled is turbulent flow around a square cylinder with edge length, H = 0.04 m. The dimensions of the domain were normalized by this edge length and can be viewed in Figure 8 and the modeling and geometry parameter values can be seen in Table 1.

The inlet boundary condition had a uniform velocity of 0.535 m/s which corresponds to a Reynolds number of 21,400. No turbulence was added at the inlet so that the results could be compared to [33-35]. The top and bottom surfaces were prescribed as walls. The left and right surfaces were prescribed as periodic boundary conditions.

The mesh had 200 nodes along the inlet and outlet walls, 290 nodes along the top and bottom wall, and 40 nodes on each of the square cylinder walls. There were 20 nodes along the channel width. The mesh was refined in the region around the square walls as well behind the cylinder to more accurately resolve the flow. The mesh can be seen in Figure 9.

Table 1: Square cylinder modeling and geometry parameters

Parameter	Value
Square Cylinder Side Length	H = 0.04 m
Inlet Velocity	U = 0.535 m/s
Reynolds Number	Re = UH/ν = 21400
Channel Width	C_W = 0.16 m
Channel Height	C_H = 0.56 m
Channel Length	C_L = 0.82 m

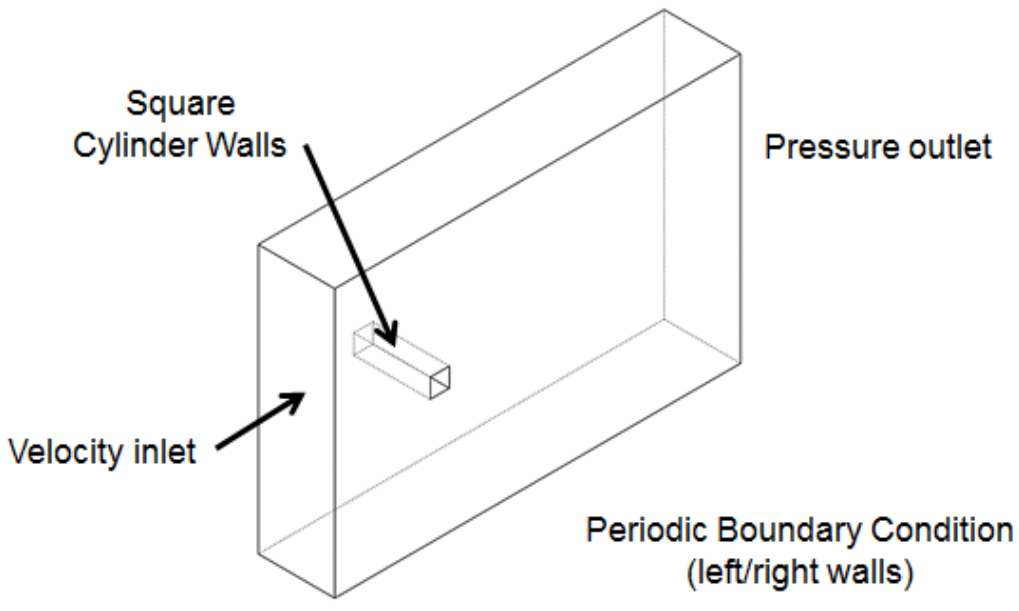

Figure 8: Square cylinder geometry

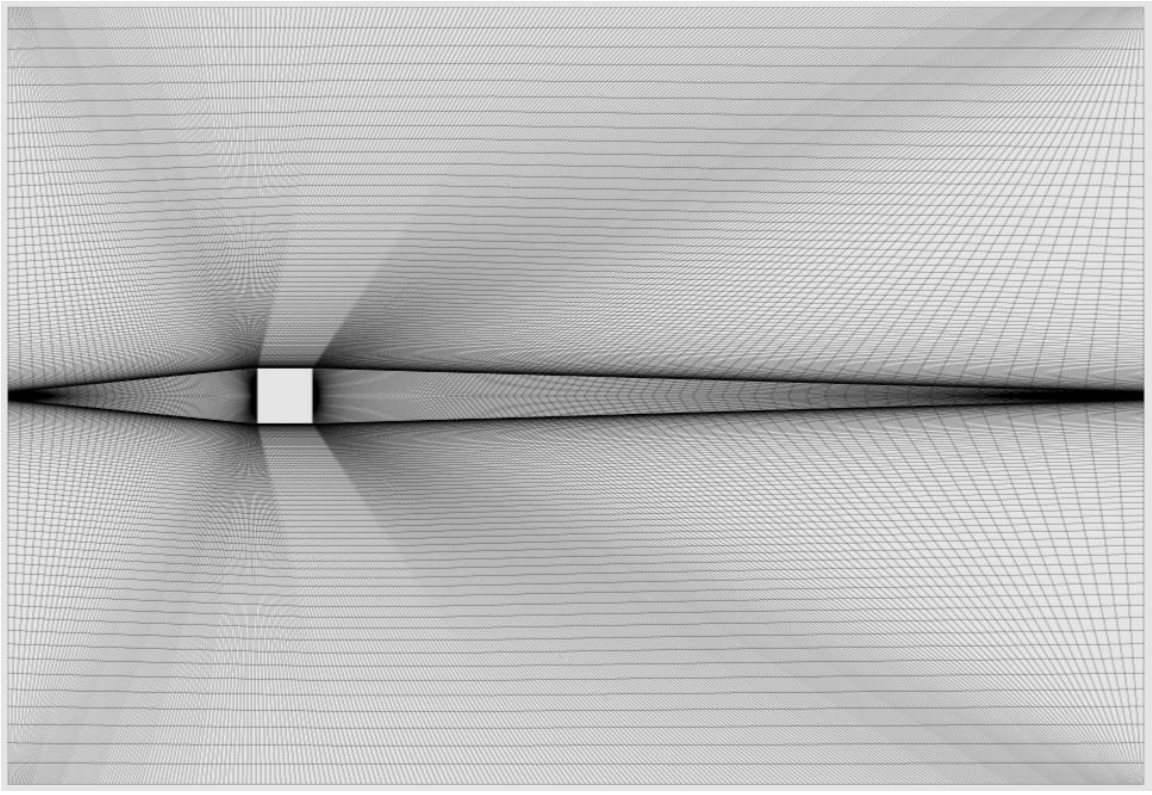

Figure 9: Square cylinder mesh of a side wall

A time step of $5(10^{-5})$ seconds was used for 39,000 time steps at 20 iterations per time step. This time step was chosen to resolve the flow using the Courant condition. The data has been averaged over 13,500 time steps using the data saved from every 500 time steps. The parameters that are compared to numerical results [33-35] include the mean lift coefficient, $\bar{C}_L$; lift oscillation amplitude, C_L^{rms}; mean drag coefficient, $\bar{C}_D$; drag oscillation amplitude, C_D^{rms}; and Strouhal number, *St*.

3.3 Shark-Skin Inspired Riblet Configurations

The methodology behind the riblet configuration setup will be explored in this section. The geometry setup, the mesh, and turbulence model parameters will be explained. There were three different blade riblet configurations that were modeled. These cases varied in the lateral spacing (s^+) and can be seen in Table 2. The other riblet parameters had a constant ratio of $\text{height/spacing} = 0.5$ and $\text{thickness/spacing} = 0.02$.

Table 2: Blade riblet configurations

Model	Lateral Spacing (s^+)
A	4.2
B	25.6
C	47.0

3.3.1 Geometry Setup

The models were created with a specific geometry as seen in Figure 10. An approximate ratio of width (δ) to height (2δ) to length (3δ) was chosen so that turbulence would form and that the wall effects from the top and bottom surfaces would not interfere with each other. If the computational model is chosen to be too small, turbulence will not form. The models need to have a minimum spanwise and streamwise length that is scaled

by the wall. The minimum spanwise length is $\lambda_x^+ = 100$ and the minimum streamwise length is $\lambda_z^+ = 300$ [36]. For these models, a computational box was chosen to be one-and-half times larger than this minimal flow unit.

The riblets were placed on the bottom with the smooth surface on the top. This setup allowed for the shear stress over these areas to be compared to determine the drag reduction without having to create two separate models: one for a smooth surface and one for a riblet surface.

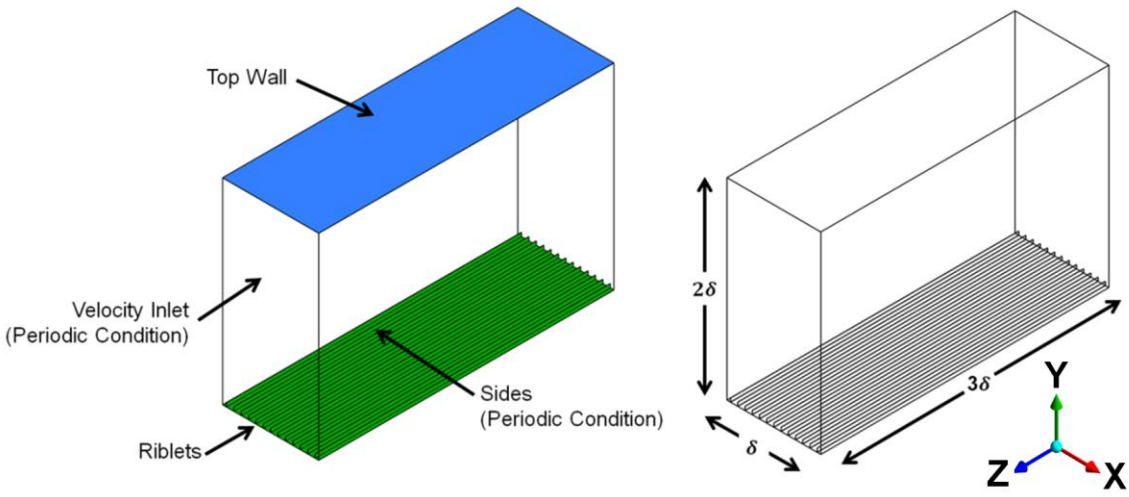

Figure 10: Geometry ratio for model setup with surfaces labeled

The riblets have specific dimensions for spacing, height, and thickness. In these models, the spacing was variable with constant ratio of *h/s* = 0.5 and *t/s* = 0.02. These parameters were chosen because they could be compared to previous experimental results.

A Reynolds (Re) number of 4200 was chosen for all models. This value influenced the dimensions of the model geometry as described below. Furthermore, this Re number was chosen for several reasons. For one, it is a turbulent value and outside of the transition from the laminar to turbulent regime. Secondly, this value is commonly used in previous experimental and computational work. Choosing the same Re number would allow for the results to be compared.

From literature, there are various equations to calculate the Re number for this geometry with similar Re number results. To match with [37], it was defined by Eq. (12) and could be used to calculate the flow rate using the geometry and fluid properties. The flow rate was then converted to mass flow rate for Fluent. To estimate the s^+ value, Eq. (12-15) were solved and inputted into Eq. (16). The expanded form of the nondimensionalized spacing equation is shown. By manipulating the x-dimension length and the number of riblets, which controlled the hydraulic diameter, various s^+ could be created from theoretical calculations.

$$\text{Reynolds Number} = \text{Re} = \frac{3Q}{4\nu L_x} = \frac{U_l \delta}{\nu} \tag{12}$$

$$\text{Hydraulic Diameter} = H_d = \frac{4A}{P} \tag{13}$$

$$\text{Wall Shear Stress} = \tau_0 = 0.03955 \nu^{\frac{1}{4}} \rho V^{\frac{7}{4}} H_d^{-\frac{1}{4}} \tag{14}$$

$$\text{Shear Stress Velocity} = V_\tau = \left(\frac{\tau_0}{\rho}\right)^{0.5} \tag{15}$$

$$\text{Nondimensionalized Spacing} = s^+ = \frac{sV_\tau}{\nu} = 0.1989 s V^{\frac{7}{8}} \nu^{-\frac{7}{8}} H_d^{-\frac{1}{8}} \tag{16}$$

3.3.2 Mesh Setup

A structured mesh was used in each computational model. The front face of the model was meshed as a map and swept through creating a structured hexagonal mesh. The number of nodes for each edge is given in Table 3 for a total of approximately 1.5 million nodes. This information can be seen on a model in Figure 11. Some of these parameters required a range for successful mesh generation due to the software not allowing for the same values to be kept. For the parameters that have a bias, a bias towards the ends was added to increase the number of elements near the wall. A higher resolution was needed near the walls for an accurate model. For the LES model, a $y^+ = 1$ is required [25]. These values from Table 3 give a greater resolution than other models [37, 38]; however, when using their mesh geometry, the solution would diverge. To get the model to converge, a mesh with a finer resolution was required. The sweep parameter was kept the same because doubling the number of divisions to 32 would not significantly change the solution [37]. In addition, keeping the number of nodes down would decrease the solution time.

Table 3: Specifications for mesh generation

	Number of Elements	Bias
Entire Model Height	175-200	100
Riblet Height	25-30	5-10
Spacing Between Riblets	30	10-20
Riblet Tips	3-5	-
Sweep	16	-

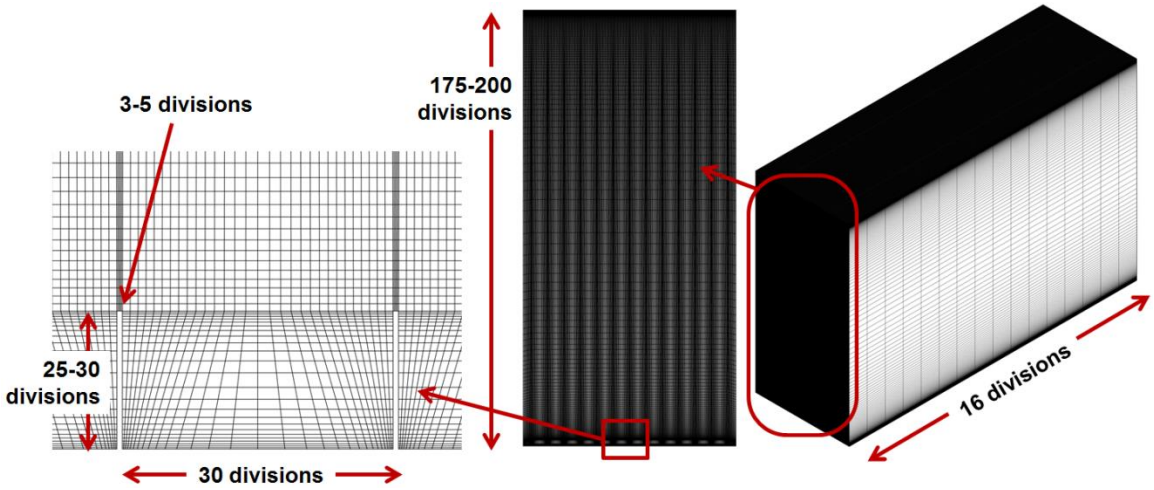

Figure 11: Description of mesh; (left) one riblet channel, (middle) velocity inlet view of model, (right) isometric view of model

3.3.3 Turbulence Model Setup

3.3.3.1 Steady State versus Transient

A transient setup was required due to the random nature of the vortices. To view the vortex formations, the solutions at discrete moments in time need to be solved. A steady state setup would not show the vortex formations. This effect was seen when the cases were solved using a steady state setup. For the transient setup, a computational time step of $(\Delta t U_l)/\delta = 0.05$ was chosen where U_l is the centerline velocity for a laminar plane channel flow with the same bulk velocity ($U_l = 1.5U_b$) and δ is the channel width. This time step was the same as [37] because the number of sweep divisions was the same. Within each time step, 20 iterations were solved.

3.3.3.2 Turbulence Model Choice

Several models were tested to see how they would perform in creating vortices. The k-epsilon, k-omega, Reynolds Stress, and Large Eddy Simulation models were tested. The k-epsilon and k-omega models were tested, and they resulted in solutions

without any vortex formations and appeared incorrect when velocity vectors were plotted. The Reynolds Stress model diverged immediately and after several tests was abandoned. The LES model was the only model that showed vortex formations; therefore, this model was used for the test cases.

3.3.3.3 Boundary Conditions

For the inlet and outlet faces as well as the left and right faces of the model, a translational periodic boundary condition was applied. This boundary condition would remove wall effects. When a fluid particle reaches the face, it comes back into the model on the matching face. This setup would allow for the turbulence and vortices to build up and form. Along the streamwise direction, a mass flow rate boundary condition was given based on the geometry and Reynolds Number. The top and bottom faces of the model, corresponding to the flat surface and riblet surface, were specified to be walls with a no-slip condition.

3.3.3.4 Solution Methods

The solution methods were left as defaults using the SIMPLE scheme, least squares cell based gradient, standard pressure, and bounded central differencing for momentum. The transient formulation was chosen to be bounded second order implicit so that a fixed time step could be chosen.

3.3.3.5 Monitors

All residuals were modified to have an absolute criterion of 10^{-6}. This value was chosen to give an accurate enough solution for each time step. Two surface monitors were created to view the integral wall shear stress on the top flat surface and the riblet

surface. These surface monitors would allow for the percentage drag difference between the two surfaces to be compared at various time steps.

3.3.3.6 Solution Initialization

The solution was initialized with zero conditions for x-velocity, y-velocity, and z-velocity. As the solution was solved, turbulence would build up. After some period of time, the vortex formations and drag change could be seen.

3.4 Post-Processing

To view the vortex formations in the model, first a new plane had to be generated that was normal to the fluid flow. Upon this plane, a vector plot of tangential velocity vectors was plotted. The vectors were colored based on the local vector velocity and were normalized in length. Approximately 50,000 equally spaced vectors were plotted to show the vortex formations.

The theoretical s^+ value was calculated from Eq. (16); however, using the model results, the actual s^+ value could be calculated using Eq. (5). The velocity far from the walls was reported by viewing a contour plot of velocity from the model and recording the maximum velocity. The drag coefficient was based off the top flat plate and was reported in Fluent. The *s* parameter was the distance between riblets and the kinematic viscosity (ν) could be calculated from the density and dynamic viscosity of the fluid.

CHAPTER 4: RESULTS AND DISCUSSION

In this section, the results from the various verification and validation test cases as well as the three blade riblet models will be presented.

4.1 Verification and Validation Test Cases

In this section, the results from the two-dimensional cylinder, driven cavity, backward facing step, and three-dimensional square cylinder will be presented and compared to the literature results.

4.1.1 Two-Dimensional Cylinder

For Reynolds numbers of 1, 20, and 100, the drag coefficient is compared to the drag coefficient for a cylinder as seen by Figure 12 and recorded in Table 4. Because the drag coefficient from Figure 12 matches well with the reported drag coefficients from Table 4, this fact shows that these models were set up correctly.

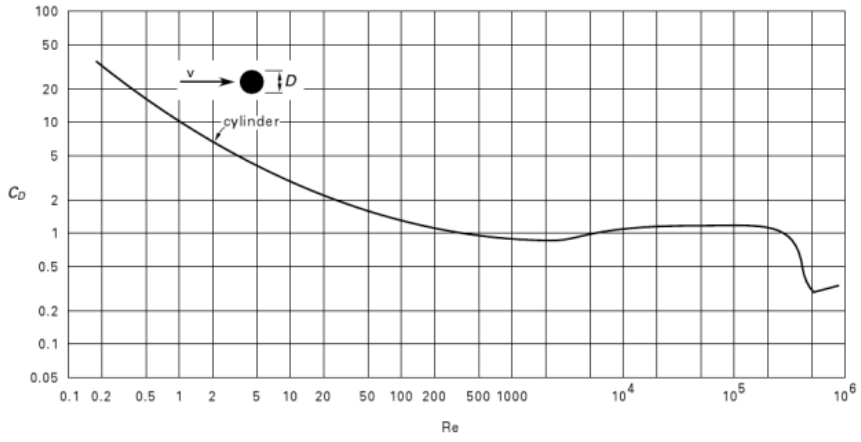

Figure 12: Drag coefficient for a smooth cylinder [39]

Table 4: Reported drag coefficient for a smooth cylinder for various Reynolds numbers

Reynolds Number	Drag Coefficient from Figure 12	Drag Coefficient from Model
1	10	11.101
20	2.2	2.0368
100	1.3	1.0843

4.1.2 Driven Cavity Flow

Data is presented for u-velocity, v-velocity, pressure, and vorticity contours plots and are compared to [26], who used a grid of 1024x1024 elements, and [27], who used a grid of 129x129 elements. The same contour line values for pressure and vorticity are used for Figure 14 and Figure 15.

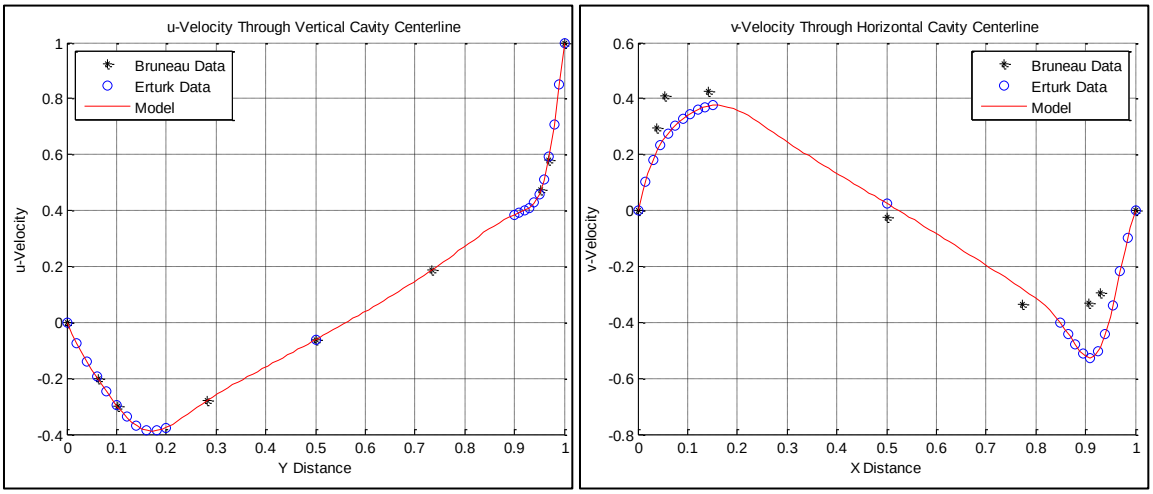

Figure 13: Driven cavity model *u*- and *v*-velocity at Re=1000;
(left) *u*-velocity at vertical cavity centerline, (right) *v*-velocity at horizontal cavity centerline

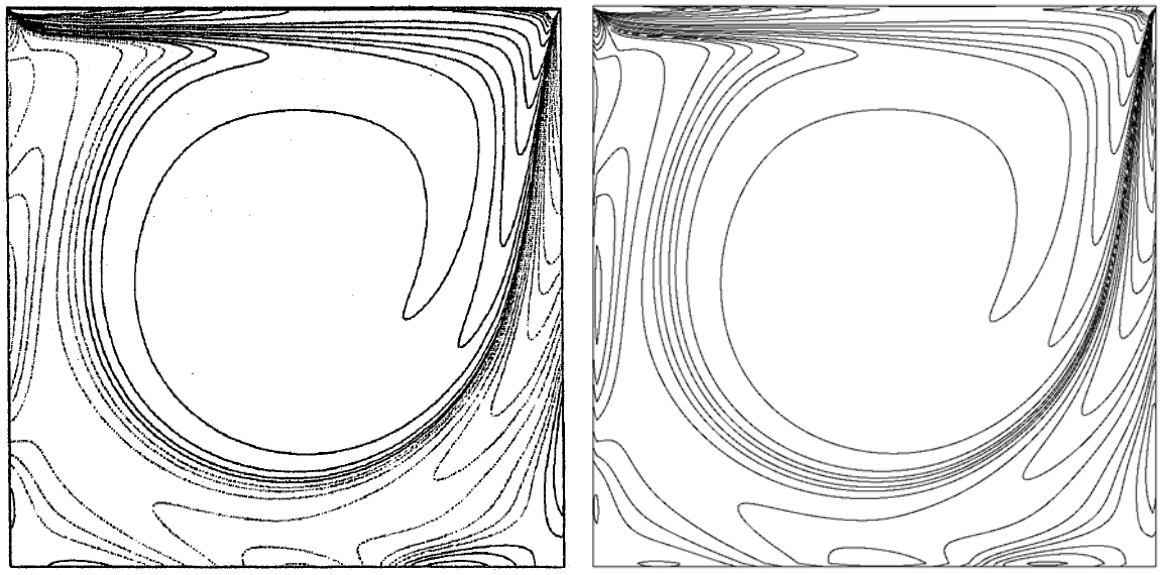

Figure 14: Driven cavity model vorticity at Re=1000 compared to [26];
(left) [26] contour plot, (right) Model contour plot

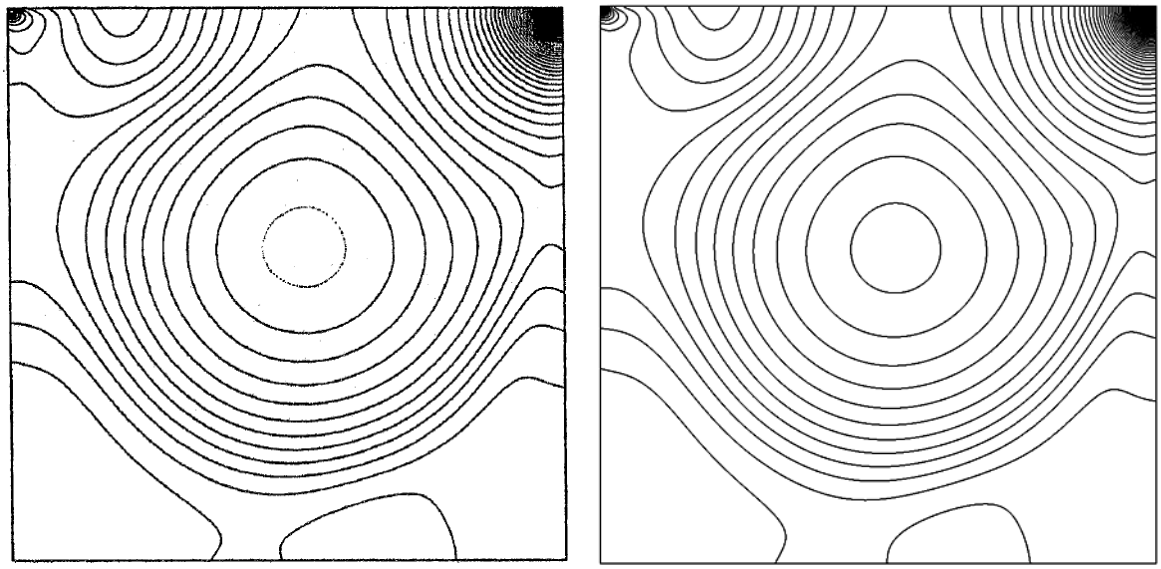

Figure 15: Driven cavity model pressure at Re=1000 compared to [26];
(left) [26] contour plot, (right) Model contour plot

From Figure 13, it can be seen that the model closely matches the data from Bruneau. The *u*-velocity through the vertical centerline matches the data from Bruneau whereas the *v*-velocity though the horizontal centerline does not match as well. This

inconsistency between plots most likely results from the differences in grid size and would decrease with mesh refinement. This statement comes from the data matching well with Erturk who used a less fine mesh.

The plot of vorticity (Figure 14) compares well to the data from Bruneau. There are only minor differences in contour lines. The plot of pressure (Figure 15) also compares well to the data from Bruneau. The only significant difference is in the upper left corner where the contour lines differ.

4.1.3 Backward Facing Step

For a Reynolds number of 800, as seen by Figure 16 and Figure 17, this model compares well with the data from [30]. The horizontal velocity profiles at the two *x* locations are nearly identical. The vertical velocity profiles at the two *x* locations have a similar profile, but do not line up as closely. This difference most likely results from a difference in mesh resolution.

Figure 18 shows the streamlines for this case and the recirculation zones can be determined from it. Each vertical black line shows one nondimensionalized spacing of $x/H = 1$. This spacing can be used to compare the detachment regions to Figure 19 as well as the data from [30] for the locations of x_1, x_4, and x_5. These spacings are shown in Table 5 and line up with these computational and experimental results.

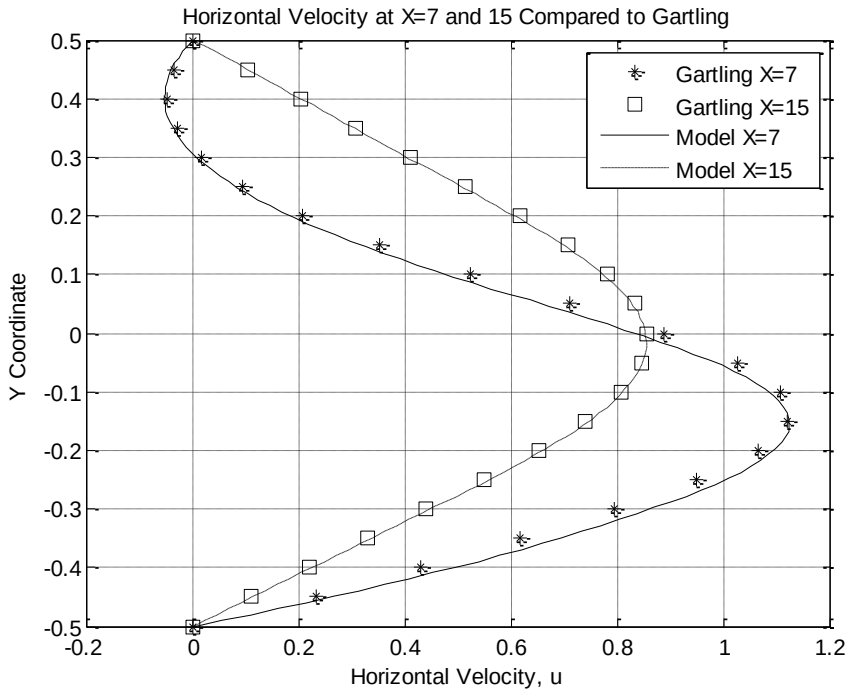

Figure 16: Horizontal velocity profiles across the channel at x=7 and 15 compared to Gartling [30]

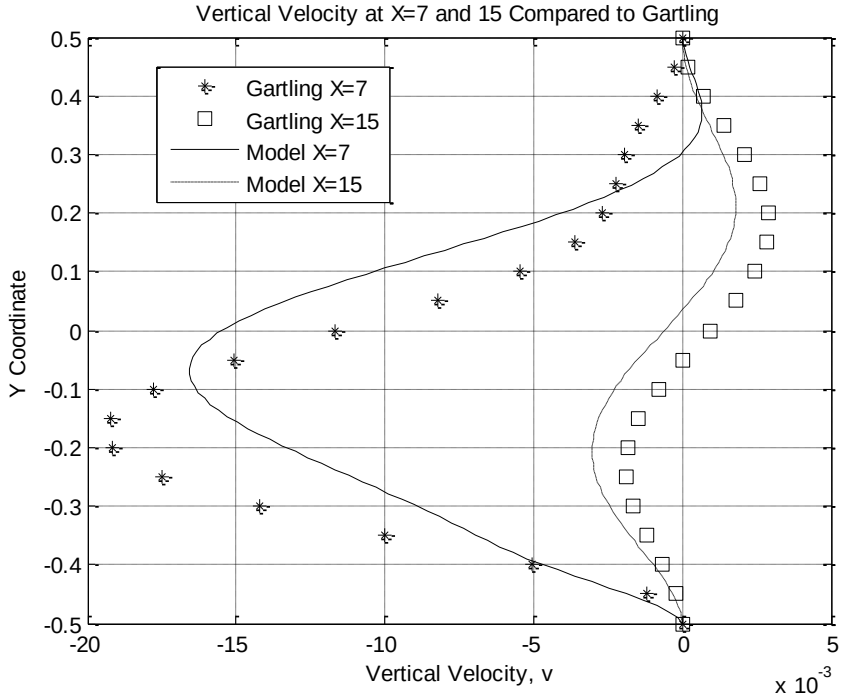

Figure 17: Vertical velocity profiles across the channel at x=7 and 15 compared to Gartling [30]

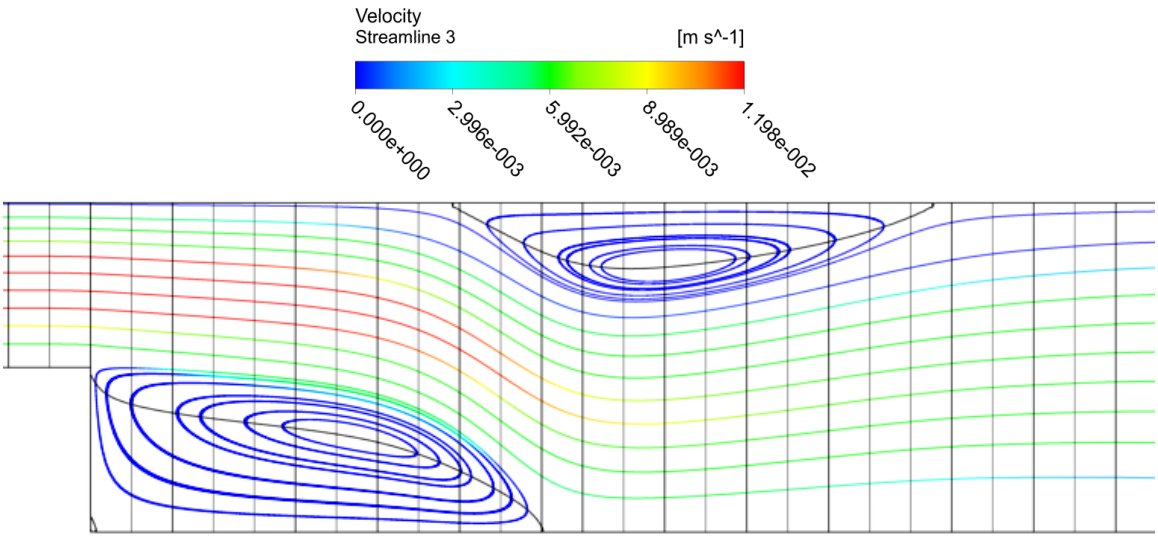

Figure 18: Streamlines for the backward facing step at Re=800 for reattachment and detachment calculation (Vertical scale expanded 4:1 for viewing ease)

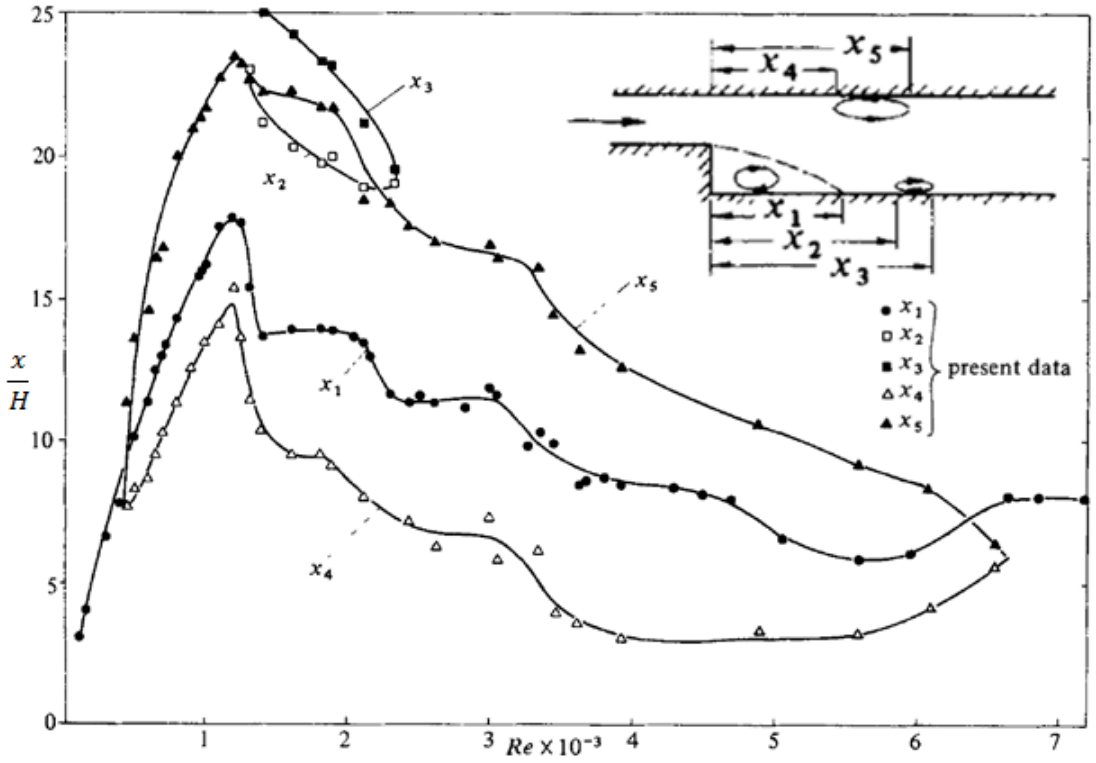

Figure 19: Location of detachment and reattachment of the flow for various locations and Reynolds numbers; Adapted from [29]

Table 5: Reattachment locations for backward facing step Re=800

Location Identifier	Spacing from Gartling	Spacing from Armaly	Spacing from Model
x_1	12	14	11.0
x_4	10	11	9.1
x_5	21	19	20.2

For the 93,000 and 210,000 Reynolds numbers, the reattachment locations were plotted and can be seen in Figure 20. Again each vertical black line shows one nondimensionalized spacing of $x/H = 1$. As seen by Table 6, the RNG k-epsilon model reports a reattachment length of 7.3 and 7.4. The accepted experimental value has a reattachment length of seven step units for both of these Reynolds numbers [31, 32]. Because these models report very similar recirculation lengths compared to the literature, it shows that these were modeled correctly.

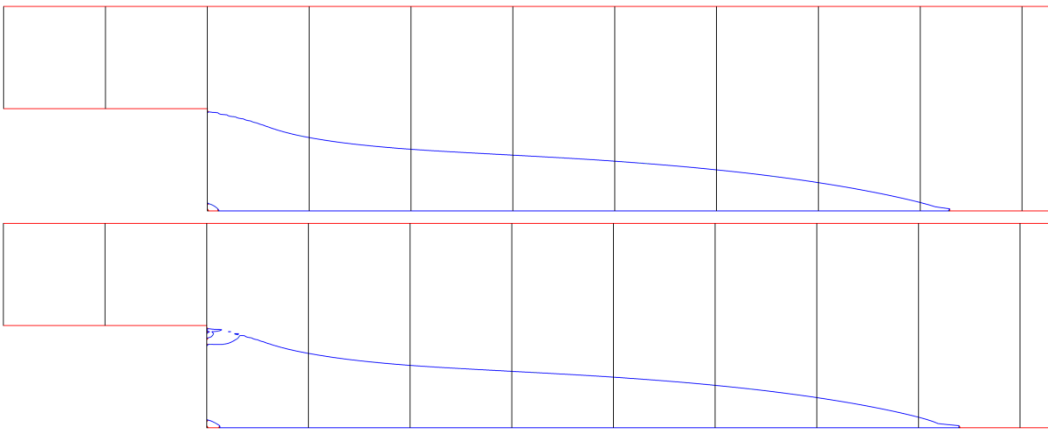

Figure 20: Reattachment location based on zero *u*-velocity for (top) Re = 93,000 and (bottom) Re = 210,000

Table 6: Reattachment location for backward facing step Reynolds of 93,000 and 210,000

Reynolds Number	**x_1 Data from Model**
93,000	7.3
210,000	7.4

4.1.4 Square Cylinder

In Table 7, mean lift coefficient, $\bar{C}_L$; lift oscillation amplitude, C_L^{rms}; mean drag coefficient, $\bar{C}_D$; drag oscillation amplitude, C_D^{rms}; and Strouhal number, *St* are compared to published numerical results. It can be seen that the drag coefficient for this work closely matches the rest of the data whereas the other values do not. The other parameters are more closely coupled to the length of time the solution is averaged. It is assumed that these values would better match the published results if the solution would run longer; however, the simulation was too time consuming and was therefore stopped.

Table 7: Comparing square cylinder data

Reference	Label	$\bar{C}_L$	C_L^{rms}	$\bar{C}_D$	C_D^{rms}	St
Ochoa [33]	GRO	0.005	1.45	2.09	0.178	0.133
	UK1	-0.02	1.01	2.2	0.14	0.13
	UK2	-0.04	1.12	2.3	0.14	0.13
	UK3	-0.05	1.02	2.23	0.13	0.13
	NT	-0.05	1.39	2.05	0.12	0.131
	UOI	0.04	1.29	2.03	0.18	0.13
	TIT	0.0093	1.39	2.62	0.23	0.131
	ST2	0.01	1.26	2.72	0.28	0.16
	ST5	0.009	1.38	2.78	0.28	0.161
	S8A	0.03	1.4	2.01	0.22	0.139
Rodi [35]	EDF_FE1	0.03	0.73	1.86	0.12	0.13
	EDF_FE2	0.007	0.38	1.66	0.10	0.066
	IIS-KOBA	-0.3	1.31	2.04	0.26	0.13
	ILLINOIS1	-0.03	1.38	2.67	0.24	0.13
	ILLINOIS2	-0.02	1.40	2.52	0.27	0.13
	KAWAMU	-0.005	1.33	2.58	0.27	0.15
	ONERA	-0.01	0.65	2.01	0.18	0.11
	UKAHY1	-0.02	1.01	2.20	0.14	0.13
	UKAHY2	-0.04	1.15	2.30	0.14	0.13
	TAMU1	-0.03	1.37	2.28	0.20	0.13
	TAMU2	-0.09	1.79	2.77	0.19	0.14
This work	MARTIN	0.14	2.19	2.28	0.38	0.11

4.2 Blade Riblet Configurations

There were three different blade riblet designs that were examined. These three models varied in their lateral spacing. The drag change and total run time is displayed in Table 8. Positive percentage drag change values correspond to increases in drag on the riblet surface. In this section, first the vortices will be discussed with respect to their size and location followed by the drag mechanisms and the run time.

Table 8: Riblet models with drag change and run time

Model	Lateral Spacing (s^+)	Percentage Drag Change	Run Time $U_\iota t/\delta$
A	4.2	0.48%	550
B	25.6	-11.9%	750
C	47.0	3.76%	1500

4.2.1 Vortex Size and Location Analysis

On a plane normal to the fluid flow, the tangential velocity vectors were plotted. These vectors are the secondary velocity vectors and were used to determine the size of the vortices. Using the nondimensional spacing between the riblets, the general size of vortices could be determined. This information can be viewed in Figure 21-22. The regions of highest velocity are shown in red; conversely, the regions of lowest velocity are shown in blue.

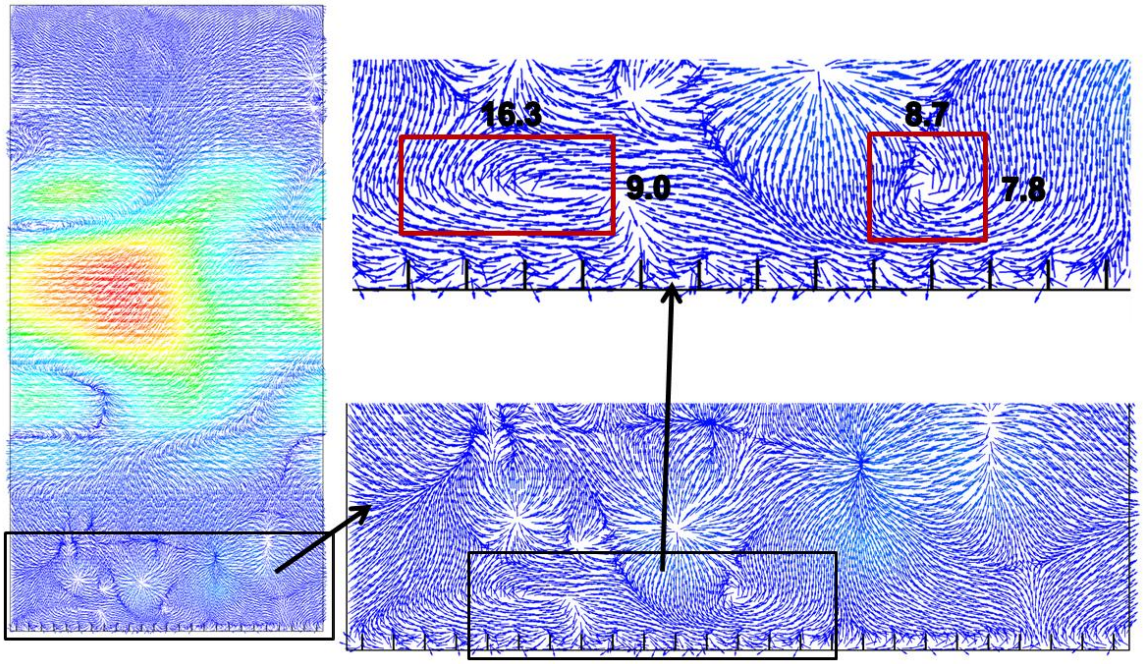

Figure 21: Secondary velocity vectors for Model A: $s^+ = 4.2$

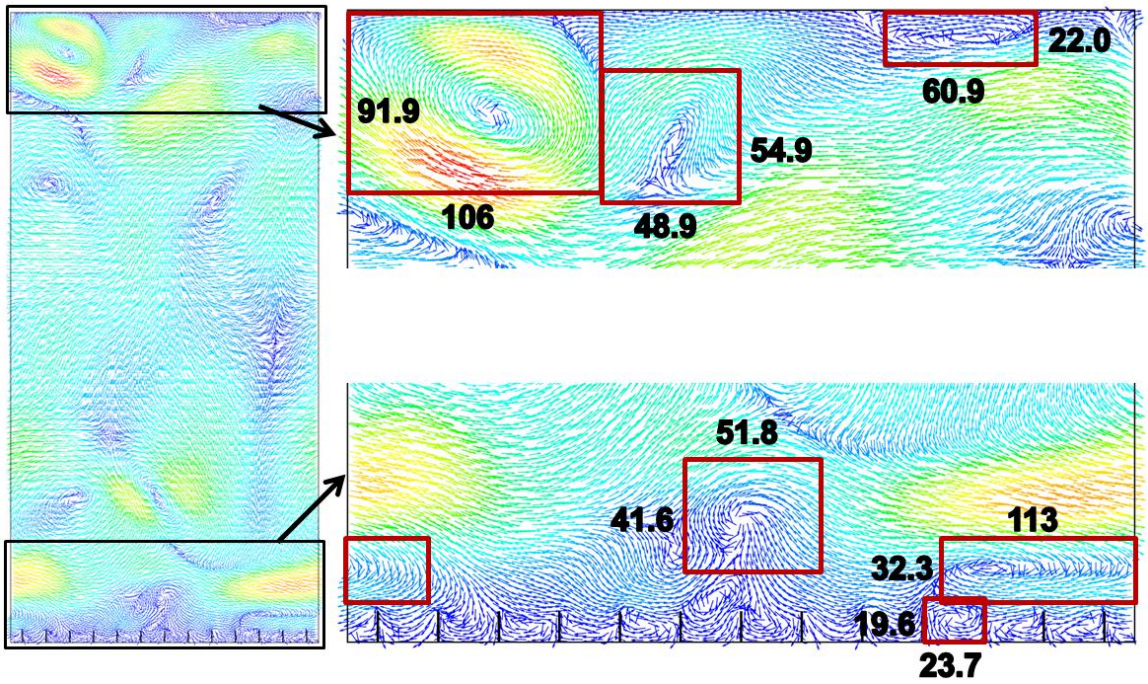

Figure 22: Secondary velocity vectors for Model B: $s^+ = 25.6$

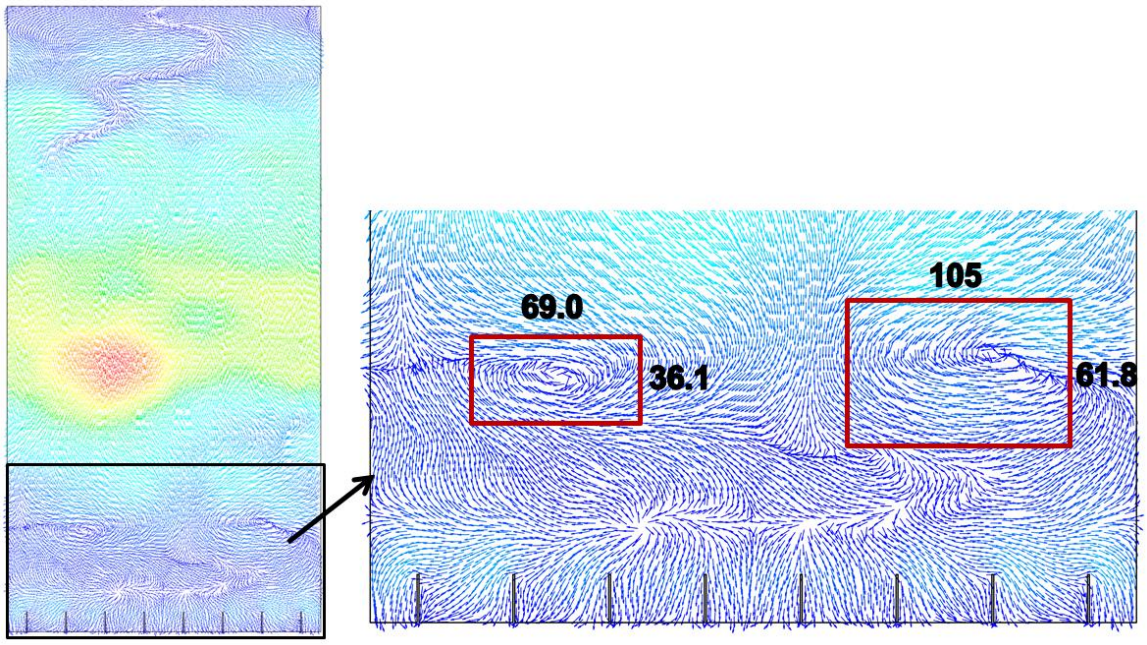

Figure 23: Secondary velocity vectors for Model C: $s^+ = 47.0$

These figures only show the vortices on one plane of each model. Because there are other vortices depending on which plane is analyzed, the size of the other vortices were calculated and are shown in Figure 24. It can be seen that there are vortices of various sizes and aspect ratios; however, the square symbols corresponding to vortices on the riblet surface, all appear below the 1:1 aspect ratio line. They also do not have a height greater than 60 wall units with the majority around 40 wall units, neglecting Model A. The vortices on the top surface did not exhibit a relationship between height and width. There were vortices with height greater than width and other vortices with width greater than height.

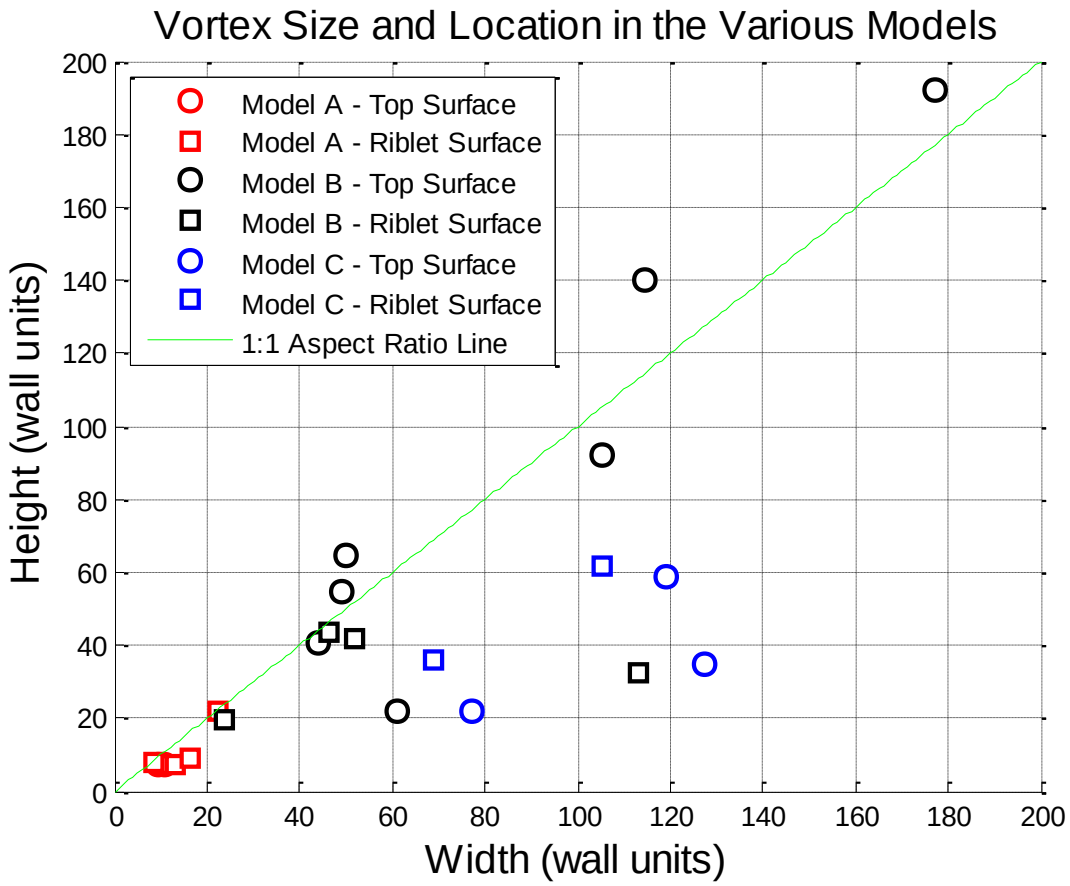

Figure 24: Vortex size and location in the various models

In addition, Figure 21 and Figure 23 have regions where fluid seems to be converging or diverging from a single location. This type of structure appears to be a region where the streamwise flow deviates or joins at a point which creates wavy streamlines. These elongated motions were commonly seen in Models A and C; however, it was rarely seen in Model B. This structure may have some effect on the reduction in integral wall shear stress because Model B had a drag reduction whereas the other two models did not.

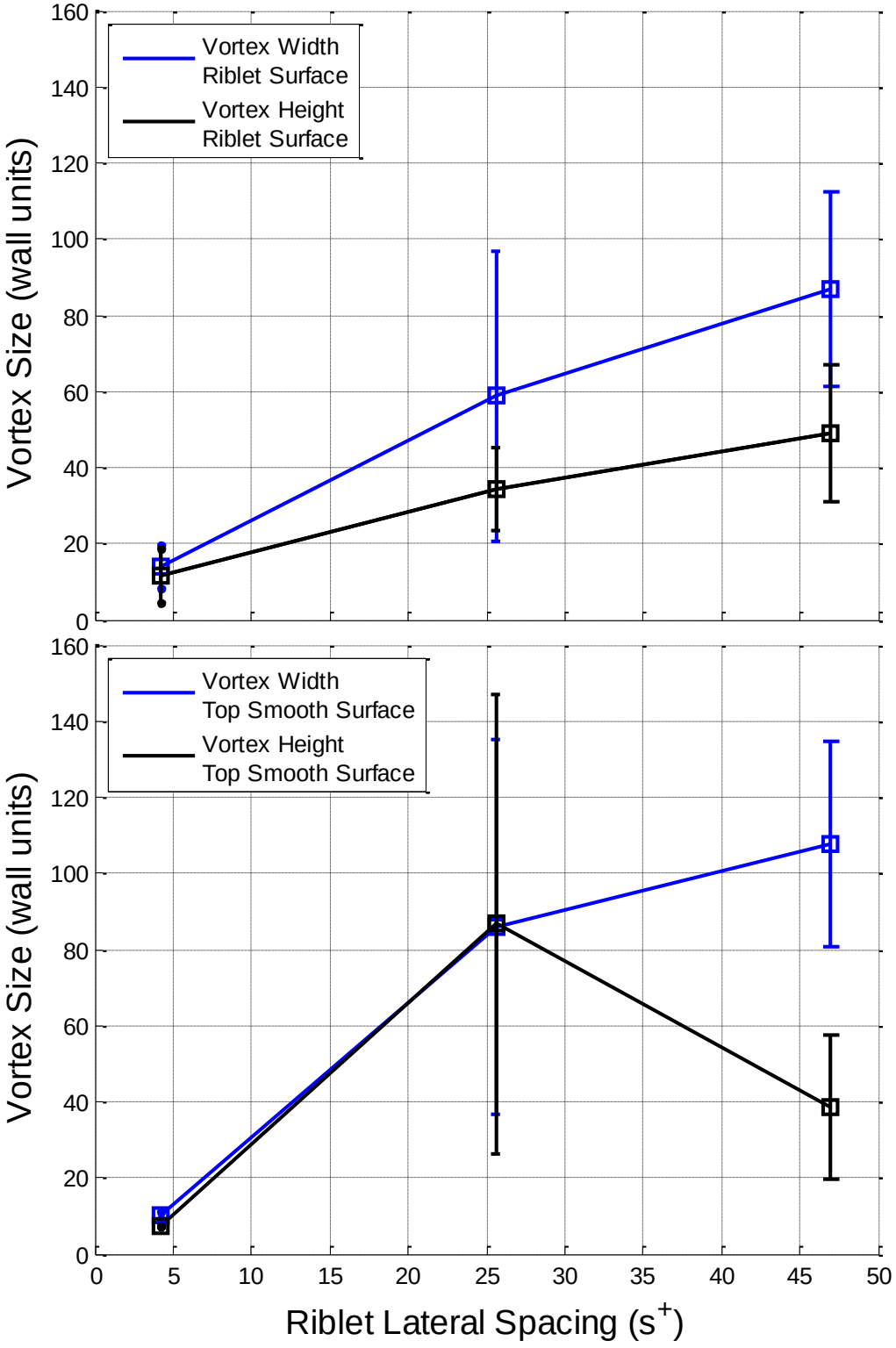

Figure 25: Vortex width and height for the riblet surface (top) and top smooth surface (bottom)

The width and height of the vortices for the riblet and top smooth surface within each model can be seen in Figure 25. It can be seen that as riblet lateral spacing increases, average vortex width and height increases for the vortices on the riblet surface. Furthermore, the vortex width increases faster than the vortex height on the riblet surface. The variation in vortex size can be seen from the large error bars. This research suggests that the vortex size (width and height) is dependent on riblet lateral spacing.

The vortices on the riblet and top smooth surface have similar size and shape for Model A. For the other two models for the top smooth surface, Model B also has square vortices whereas Model C has vortices that have a width much greater than height. Because the top surface is a flat surface and far from the riblet surface, there should not be any relationship as riblet lateral spacing changes. Further models need to be studied to explain the results from this research.

4.2.2 Drag Mechanisms Analysis

From Table 8, Model B has the greatest drag reduction with the other two models having a drag increase. This result is similar to [4] in that within a range of varying lateral spacing, there is a spacing that will show the greatest drag reduction. Model B may show a drag reduction due to the vortices being lifted away from the riblet surface. In Figure 22, there are a couple vortices that are only interacting with the riblet tips with one lower velocity vortex in the riblet valley. Because the higher velocity vectors are only interacting with the riblet rips, this would lead to a drag reduction. Furthermore, there is more dark blue, corresponding to low velocity, at the riblet surface than at the smooth surface. The vortices on the smooth surface are in direct contact with the surface.

A contour plot of shear stress for Model B is shown in Figure 26. The smooth surface has an overall higher wall shear (shown as orange); whereas, the riblet surface only has high wall shear (red) at the riblet tips with lower shear stress elsewhere. Even though the riblet has more surface area, these regions of lower shear stress decreased the total amount of force over the riblets compared to the smooth surface. The higher shear stress is due to the higher velocity fluid at these locations. The majority of the lower shear stress on the bottom surface is due to the lower velocity fluid in the riblet channels.

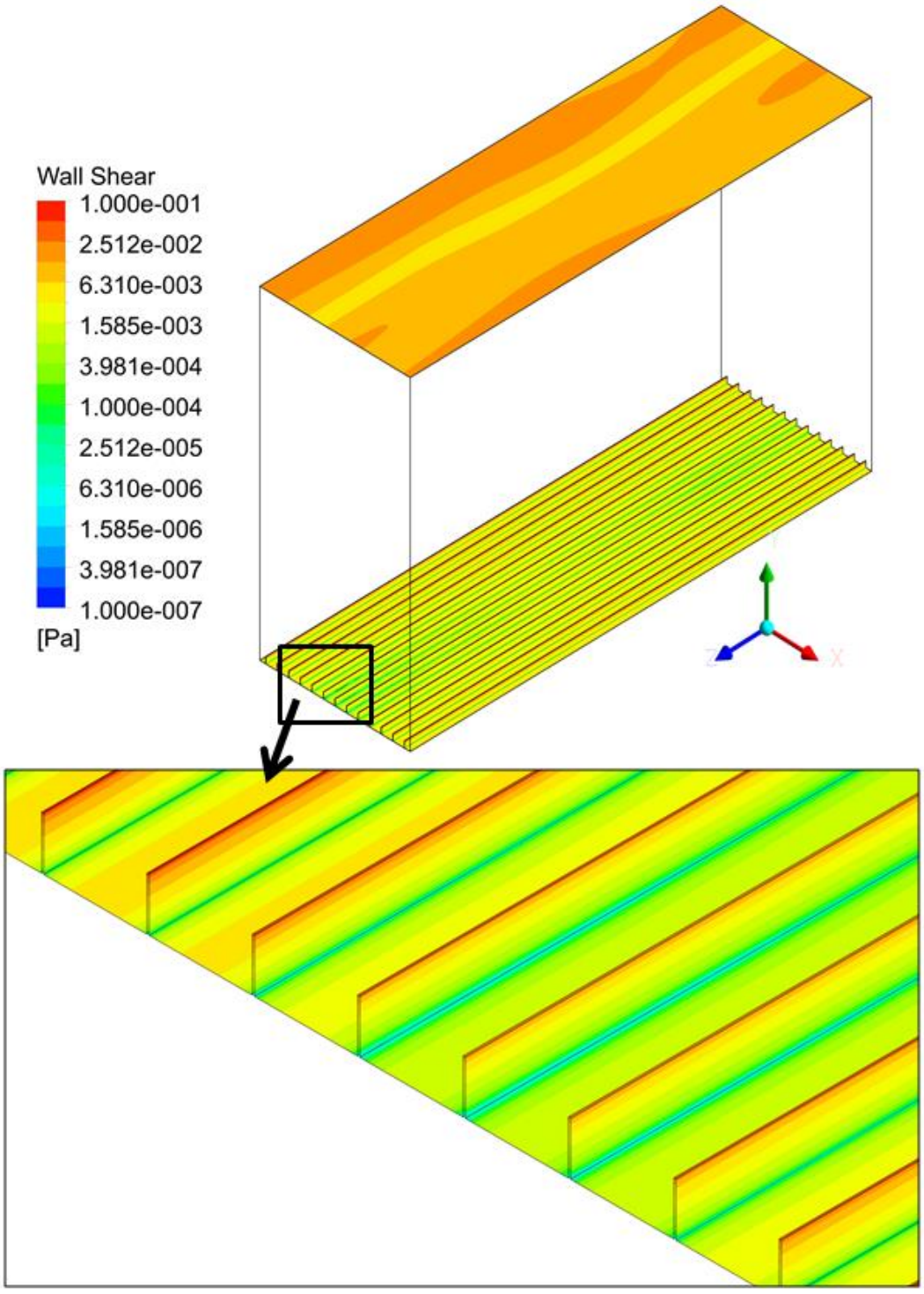

Figure 26: Plot of wall shear stress on the riblet and smooth surfaces for Model B: $s^+ = 25.6$

4.2.3 Run Time Analysis

As seen in Table 8, Model C was run for a nondimensional run time of 1500. This much longer run time was done to see the effects of increasing the number of time steps. The lateral spacing and drag change for several instances in time were saved and plotted in Figure 27. After a nondimensional time of 750, these two parameters do not vary significantly. Based on this information, at near this nondimensional time, it can be assumed that the results will not considerably change if the models are run longer.

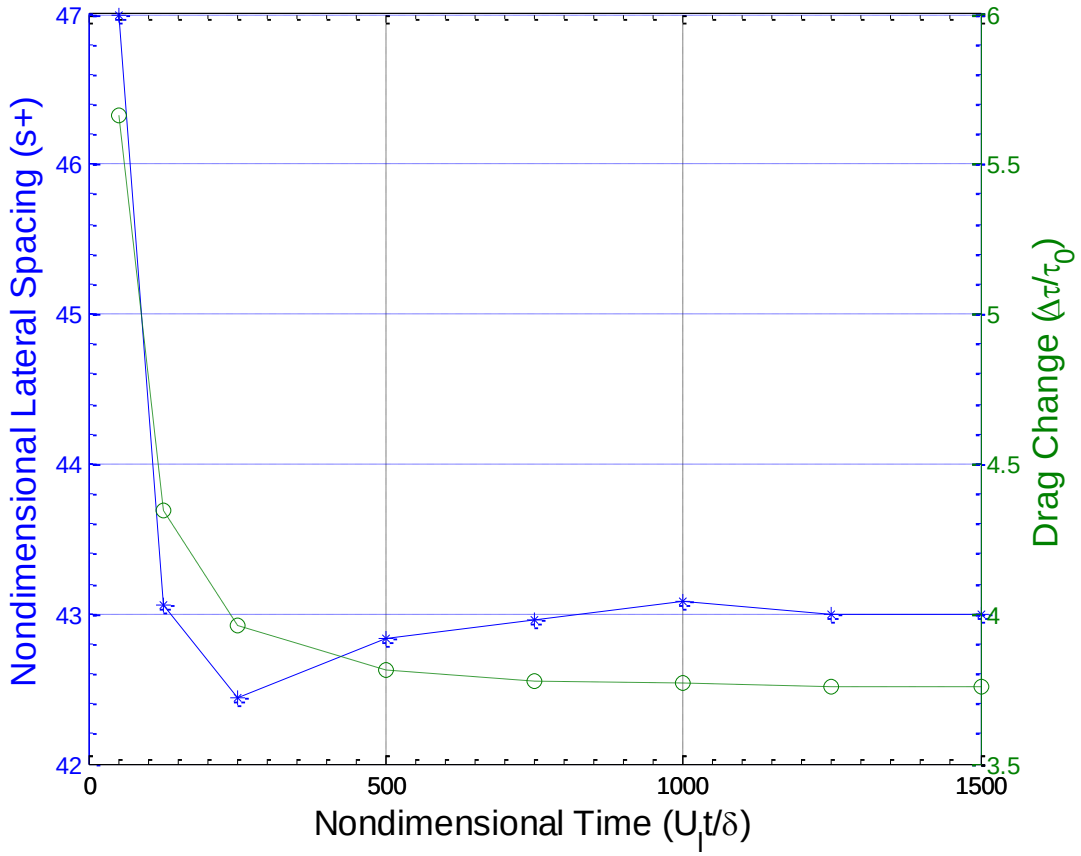

Figure 27: Lateral spacing and drag change compared to time steps for Model C: s^+ = 47.0

CHAPTER 5: CONCLUSIONS

The purpose of this research was to study vortex size, vortex location, and drag changes due to varying lateral riblet spacing compared to a smooth reference through a computational fluid dynamic analysis.

5.1 Summary

Background information on shark skin inspired surfaces were discussed which included the mechanisms of fluid drag, the role riblets play in drag reduction, and the previous research into these structures. Various computational models setup and results for verification/validation and riblet research were presented.

Previous research has shown that there is a drag reduction associated with riblet geometries that changes based on the surface profile; however, little research has been done regarding vortex size and location. This research looked into the vortex size and location for varying lateral riblet spacing. This study determined that vortices are of various sizes and aspect ratios. It was found that as riblet lateral spacing increases, the width and height of the vortices increases as well. This result needs to be further studied through more models to understand whether vortices have a constant width or a changing width to optimize riblet geometries.

5.2 Future Work

In this research, blade riblets were tested with varying lateral spacing. A large parametric study by modifying various parameters could be done. Additional two-dimensional riblet models using scalloped and sawtooth geometries or three-dimensional staggered models could also be tested. Other parameters including h^+, t^+, α, and Re could be modified. Creating more models and looking at the flow characteristics such as vortex size, shape, and location as well as drag changes would be informative in designing the next generation of riblet designs.

It is noted that using computational resources instead of experimental resources requires a large amount of computing time and processing power to simply complete one test case. If this research were to be continued using the LES model, it is suggested that an alternative initialization scheme be implemented to try to save solution time. Instead of starting the LES model from zero initial conditions, it could be started from a steady state Reynolds-averaged Navier-Stokes (RANS) turbulence model solution. If this method was attempted, the solve/initialize/init-instantaneous-vel text command needs to be executed to generate the instantaneous velocity field for the LES run. This setup should generate a more realistic initial field and reduce the time for the LES to reach a stable mode [25].

Another possible method of decreasing solution time would be to increase the Reynolds number. As Reynolds number increases, turbulence and vortex formations increase which could make it easier to view vortices and decrease the time it takes for them to form.

LIST OF REFERENCES

1. Bhushan, B., *Biomimetics: lessons from nature–an overview.* Philosophical Transactions of the Royal Society A: Mathematical, Physical and Engineering Sciences, 2009. **367**(1893): p. 1445-1486.
2. Bhushan, B., *Nanotribology and Nanomechanics: An Introduction*2008: Springer-Verlag GmbH.
3. Bhushan, B., *Springer handbook of nanotechnology*. 3 ed2010: Springer.
4. Bechert, D., et al., *Experiments on drag-reducing surfaces and their optimization with an adjustable geometry.* Journal of Fluid Mechanics, 1997b. **338**(1): p. 59-87.
5. Dean, B. and B. Bhushan, *Shark-skin surfaces for fluid-drag reduction in turbulent flow: a review.* Philosophical Transactions of the Royal Society A: Mathematical, Physical and Engineering Sciences, 2010. **368**(1929): p. 4775-4806.
6. Reif, W.E., *Squamation and Ecology of Sharks*1985: E. Schweizerbartsche Verlagsbuchhandlung.
7. Bechert, D., M. Bruse, and W. Hage, *Experiments with three-dimensional riblets as an idealized model of shark skin.* Experiments in fluids, 2000a. **28**(5): p. 403-412.
8. Munson, B.R., et al., *Fundamentals of fluid mechanics*2009: Wiley.
9. Kline, S., et al., *The structure of turbulent boundary layers.* Journal of Fluid Mechanics, 1967. **30**(04): p. 741-773.
10. Bechert, D., G. Hoppe, and W.-E. Reif. *On the drag reduction of the shark skin*. in *1985 AIAA Shear Flow Control Conference*. 1985.
11. Luchini, P., F. Manzo, and A. Pozzi, *Resistance of a grooved surface to parallel flow and cross-flow.* J. Fluid Mech, 1991. **228**(87): p. 109.
12. Lee, S.-J. and S.-H. Lee, *Flow field analysis of a turbulent boundary layer over a riblet surface.* Experiments in fluids, 2001. **30**(2): p. 153-166.
13. Rohr, J., et al., *A comparison of the drag-reducing benefits of riblets in internal and external flows.* Experiments in fluids, 1992. **13**(6): p. 361-368.

14. Walsh, M.J., *Riblets as a viscous drag reduction technique.* AIAA journal, 1983. **21**(4).

15. Walsh, M.J., *Drag characteristics of V-groove and transverse curvature riblets.* Viscous flow drag reduction, 1980: p. 168-184.

16. Walsh, M.J. *Turbulent boundary layer drag reduction using riblets*. in *AIAA, Aerospace Sciences Meeting*. 1982.

17. Bechert, D., et al. *Drag reduction mechanisms derived from shark skin*. in *IN: ICAS, Congress, 15th, London, England, September 7-12, 1986, Proceedings. Volume 2 (A86-48976 24-01). New York, American Institute of Aeronautics and Astronautics, Inc., 1986, p. 1044-1068.* 1986.

18. Bechert, D., et al., *Fluid mechanics of biological surfaces and their technological application.* Naturwissenschaften, 2000b. **87**(4): p. 157-171.

19. Wilkinson, S.P., et al., *Turbulent drag reduction research at NASA langley: progress and plans.* International Journal of Heat and Fluid Flow, 1988. **9**(3): p. 266-277.

20. Wilkinson, S. and B. Lazos. *Direct drag and hot-wire measurements on thin-element riblet arrays*. in *IUTAM, Symposium on Turbulence Management and Relaminarization, Bangalore, India, Jan. 19-23, 1987, Paper. 12 p.* 1987.

21. Lang, A., et al., *Bristled shark skin: a microgeometry for boundary layer control?* Bioinspiration & biomimetics, 2008. **3**(4): p. 046005.

22. Jung, Y.C. and B. Bhushan, *Biomimetic structures for fluid drag reduction in laminar and turbulent flows.* Journal of Physics: Condensed Matter, 2009. **22**(3): p. 035104.

23. Bechert, D., et al., *Biological surfaces and their technological application-laboratory and flight experiments on drag reduction and separation control.* AIAA paper, 1997a. **1960**.

24. America, A.f. *A4A Jet-Fuel Cost and Consumption Report*. 2013 January 4, 2013]; Available from: http://www.airlines.org/Pages/A4A-Jet-Fuel-Cost-and-Consumption-Report.aspx.

25. Fluent, *Fluent V14.0 Help Files.* 2013.

26. Bruneau, C.-H. and M. Saad, *The 2D lid-driven cavity problem revisited.* Computers & fluids, 2006. **35**(3): p. 326-348.

27. Erturk, E., T.C. Corke, and C. Gökçöl, *Numerical solutions of 2-D steady incompressible driven cavity flow at high Reynolds numbers.* International Journal for Numerical Methods in Fluids, 2005. **48**(7): p. 747-774.

28. Kim, S.-W., *A fine grid finite element computation of two-dimensional high Reynolds number flows.* Computers & fluids, 1988. **16**(4): p. 429-444.

29. Armaly, B., et al., *Experimental and theoretical investigation of backward-facing step flow*. J. Fluid Mech, 1983. **127**(473): p. 20.

30. Gartling, D.K., *A test problem for outflow boundary conditions—flow over a backward-facing step.* International Journal for Numerical Methods in Fluids, 1990. **11**(7): p. 953-967.

31. Nallasamy, M. and C. Chen, *Studies on effects of boundary conditions in confined turbulent flow predictions.* NASA STI/Recon Technical Report N, 1985. **85**: p. 35371.

32. Kim, J.J., *Investigation of separation and reattachment of a turbulent shear layer: flow over a backward-facing step.* 1978.

33. Ochoa, J. and N. Fueyo, *Large Eddy Simulation of the flow past a square cylinder*. PHOENICS Journal of Computational Fluid Dynamics and its Applications, 2004. **17**.

34. Rodi, W., *Comparison of LES and RANS calculations of the flow around bluff bodies.* Journal of Wind Engineering and Industrial Aerodynamics, 1997. **69**: p. 55-75.

35. Rodi, W., et al., *Status of large eddy simulation: results of a workshop.* Transactions-American Society of Mechanical Engineers Journal of Fluids Engineering, 1997. **119**: p. 248-262.

36. Jimenez, J. and P. Moin, *The minimal flow unit in near-wall turbulence.* Journal of Fluid Mechanics, 1991. **225**(213-240).

37. Choi, H., P. Moin, and J. Kim, *Direct numerical simulation of turbulent flow over riblets.* Journal of Fluid Mechanics, 1993. **255**: p. 503-503.

38. Chu, D.C. and G.E. Karniadakis, *A direct numerical simulation of laminar and turbulent flow over riblet-mounted surfaces.* Journal of Fluid Mechanics, 1993. **250**(1): p. 1-42.

39. Lindeburg, M.R., *Mechanical engineering reference manual*1994: Professional Publications.